

Accepted Manuscript

Stress evolution and structural inheritance controlling an intracontinental extensional basin: The central-northern sector of the Neogene Teruel Basin

Carlos L. Liesa, José L. Simón, Lope Ezquerro, Luis E. Arlegui, Aránzazu Luzón



PII: S0191-8141(18)30378-X

DOI: <https://doi.org/10.1016/j.jsg.2018.11.011>

Reference: SG 3778

To appear in: *Journal of Structural Geology*

Received Date: 13 July 2018

Revised Date: 2 November 2018

Accepted Date: 17 November 2018

Please cite this article as: Liesa, C.L., Simón, José.L., Ezquerro, L., Arlegui, L.E., Luzón, Ará., Stress evolution and structural inheritance controlling an intracontinental extensional basin: The central-northern sector of the Neogene Teruel Basin, *Journal of Structural Geology* (2018), doi: <https://doi.org/10.1016/j.jsg.2018.11.011>.

This is a PDF file of an unedited manuscript that has been accepted for publication. As a service to our customers we are providing this early version of the manuscript. The manuscript will undergo copyediting, typesetting, and review of the resulting proof before it is published in its final form. Please note that during the production process errors may be discovered which could affect the content, and all legal disclaimers that apply to the journal pertain.

1 **Stress evolution and structural inheritance controlling an intracontinental**
2 **extensional basin: the central-northern sector of the Neogene Teruel Basin**

3 **Carlos L. Liesa*, José L. Simón, Lope Ezquerro, Luis E. Arlegui, Aránzazu Luzón**

4 *Departamento de Ciencias de la Tierra, Facultad de Ciencias, Grupo Geotransfer-Instituto de*
5 *Investigación en Ciencias Ambientales (IUCA), Universidad de Zaragoza, Pedro Cerbuna 12,*
6 *50009 Zaragoza, Spain*

- 7 • Carlos L. Liesa (carluis@unizar.es) * (Corresponding author)
8 • José L. Simón: jsimon@unizar.es
9 • Lope Ezquerro: lope@unizar.es
10 • Luis E. Arlegui: arlegui@unizar.es
11 • Aránzazu Luzón: aluzon@unizar.es

12 **Abstract**

13 The Teruel Basin is a NNE-SSW trending intracontinental extensional basin located in central-
14 eastern Iberia. It is asymmetrically bounded to the east by a major fault zone, but intrabasinal
15 faults with diverse orientation (NNE-SSW to NE-SW, E-W, or NW-SE) also appear. Offsets of
16 the successive sedimentary units and of two planation surfaces reveal that tectonic activity
17 initiated at the border faults, while intrabasinal ones mainly developed in a later stage. Fractures
18 on a map scale show a prevailing N-S strike in Neogene synrift rocks, while a dense network
19 made of four main fracture sets (NE-SW, E-W to ESE-WNW, N-S and NNW-SSE), likely
20 inherited from Mesozoic rifting stages, is observed in pre-rift units. The results of palaeostress
21 analyses indicate an overall predominance of σ_3 directions around E-W, although two stress

22 episodes have been distinguished during the Late Miocene-Pleistocene: (i) triaxial extension with
23 σ_3 E-W; (ii) almost 'radial' extension (σ_1 vertical, $\sigma_2 \approx \sigma_3$) with a somehow prevailing σ_3 ENE-
24 WSW. A scenario in which the evolving extensional stress field was able to gradually activate
25 major basement structures with different orientation, inherited from previous tectonic events, is
26 proposed as responsible for the evolution and overall pattern of both the eastern active margin
27 and central parts of the central-northern sector of the Teruel Basin.

28 **Keywords:** fracture; paleostress; stress partitioning; normal fault; extensional basin

29 **1. Introduction**

30 Evolution of active extensional basin margins has been mainly analysed in the light of
31 numerical, analogue or natural models that pay attention to fault interaction and linkage (e.g.
32 Peacock and Sanderson, 1991; Crider and Pollard, 1998; Walsh et al., 1999; Gupta and Scholz,
33 2000). In most of these models it is assumed that a pre-existing homogeneous rock mass is
34 subjected to a steady-state stress field to produce faults. However, it is more realistic to expect
35 stress fields that change over time and the influence of pre-existing structures in underlying and
36 adjacent rocks.

37 Development of fracture systems that control extensional basins should be seen in the
38 framework of tectonic stress fields that are heterogeneous both in space and time, due to (i)
39 intrinsic variability of stress sources, (ii) local perturbations, and (iii) rheological contrasts
40 (Caputo, 2005). Changes in tectonic framework could produce changes in the 'local' stress field,
41 hence inducing apparent 'phases' as inferred from distinct fault systems. Deflection of stress
42 trajectories is caused either directly by slip along faults or undirectedly due to mechanical
43 discontinuities (e.g. Rispoli, 1981; Homberg et al., 1997; Simón et al., 1999). Its effect is
44 maximum close to fractures where the resolved shear stress regularly tend to 0 during each
45 seismic cycle and the direction of the maximum horizontal stress (S_{Hmax}) is deflected to become

46 either nearly parallel or nearly orthogonal to the faults (Simón et al., 1988). Relative variations of
47 also the principal stress magnitudes frequently result in permutation or interchange of stress axes
48 (owing to either gradual change in remote stress magnitudes, or release of stress normal to
49 primary fractures subsequent to failure under unvarying remote stress conditions; e.g. Larroque
50 and Laurent, 1988; Bai et al., 2002). Finally, *stress partitioning* represents a further type of stress
51 heterogeneity, conceptually different from both random stress variability, and ‘polyphase’
52 tectonics. It appears as systematic, sometimes cyclically sequenced records of distinct stress
53 fields, giving the appearance that the total stress field is decoupled into several components
54 (Simón et al., 2008).

55 The Neogene Teruel Graben is a noteworthy case of extensional basin developed through
56 varying stress conditions and strongly influenced by structural inheritance. Recent extensional
57 stress fields in the region were initially reconstructed by Simón (1982, 1983, 1989), then
58 refined by Cortés (1999), Liesa (2000, 2011a) and Lafuente (2011). Arlegui et al. (2005, 2006)
59 made an important contribution to that reconstruction by processing abundant fault population
60 data without striation orientations, by using the method proposed by Lisle et al. (2001). The
61 model resulting from such research is a complex regional stress field that evolved through
62 Neogene following three main stages: (i) nearly N-S compression active until Middle Miocene,
63 with σ_1 trajectories frequently flipping between NNW-SSE and NNE-SSW trends; (ii) triaxial
64 extension with σ_3 trajectories oriented W-E to WNW-ESE, prevailing during the Late Miocene;
65 (iii) almost radial extension (σ_1 vertical, $\sigma_2 \approx \sigma_3$) with a generally prevailing σ_3 trending nearly
66 WSW-ENE, mainly since late Pliocene, which commonly undergoes stress deflections,
67 permutations and partitioning.

68 The evolutionary pattern of faults and fractures (generated during specific tectonic
69 episodes, later reactivated controlling new structural settings) was firstly established by Simón
70 (1983, 1989). More detailed analysis of fracture systems, mainly those present in El Pobo Range

71 (east of the Teruel Graben), is due to Liesa (2000, 2011b). The imprint of inherited structures
72 along the tectonic evolution of the region has been revealed by e.g. Liesa et al. (2006) for
73 Mesozoic extensional basins of the Maestrazgo domain, Liesa et al. (2004) or Lafuente et al.
74 (2011) for Palaeogene contractional structures, and Rubio and Simón (2007) for recent
75 extensional faults.

76 Recently, the PhD study by Ezquerro (2017) has compiled existing information and added
77 new data. The entire data set was analysed with the aim of building an evolutionary model for
78 the Teruel Basin, in which structural, sedimentary, paleoclimatic, geomorphological and
79 chronological aspects are fully integrated. The present paper summarizes the main results of that
80 unpublished regional study (Ezquerro, 2017) focusing on stress fields and fracture evolution. In
81 particular, our main goal is to show the role of the inherited pre-rift structures during the basin
82 evolution, and demonstrate how a spatially and temporally heterogeneous stress field selectively
83 reactivated these pre-existing structures.

84 **2. Geological setting**

85 The Neogene, NNE-SSW trending Teruel Basin is located in the central-eastern Iberian
86 Chain (Fig. 1a), cutting obliquely and postdating the Alpine contractional structures (Álvaro et
87 al., 1979). It represents the main onshore structure linked to the Valencia Trough rifting (Simón,
88 1982), belonging to an extensional fault system detached at a depth of 11-14 km (Roca and
89 Guimerà, 1992). This fault system evolved through two distinct extensional episodes (Simón,
90 1982, 1983): the first one (Miocene) gave rise to the main NNE-SSW trending grabens (Teruel
91 and Maestrazgo), and the second one (Late Pliocene-Quaternary) originated the NNW-SSE
92 trending Jiloca graben and partly reactivated the Teruel and Maestrazgo structures.

93 The northern Teruel Basin was filled in endorheic conditions by a continuous sedimentary
94 succession made of alluvial, palustrine, lacustrine and aeolian facies, ranging from Late Miocene

95 (Vallesian) to Late Pliocene (Villafranchian) in age (e.g. Simón, 1983; Alcalá et al., 2000;
96 Rodríguez-López et al., 2012). These deposits have been divided into four formal
97 lithostratigraphical units (Peral, Alfambra, Tortajada and Escorihuela Formations; Weerd, 1976),
98 as well as into informal units (*Unidad Detrítica Inferior-Rojo 1, Calizas Intermedias, Páramo 1,*
99 *Rojo 2, Páramo 2, Rojo 3* and *Villafranchian Pediment*; Godoy et al., 1983a,b), and genetic units
100 (Alonso-Zarza and Calvo, 2000). More recently, Ezquerro (2017) has defined six genetic units
101 (TN1 to TN6) based on an overall megasequential evolution mainly controlled by tectonics.

102 The northern sector of the Teruel Basin is a halfgraben bounded by the N-S striking El
103 Pobo Fault Zone (EPFZ) (Fig. 1b). The footwall block (El Pobo Range) consists of Triassic and
104 Jurassic rocks, deformed by interfering NW-SE and NE-SW trending folds and a dense fault grid
105 (Liesa, 2000, 2011a,b; Liesa et al., 2006; Antolín-Tomás et al., 2007). The Neogene infill in the
106 hanging-wall block began during Middle Miocene (Tortonian) times and lay on a widespread
107 planation surface, the *Intramiocene Erosion Surface (IES)* (Gutiérrez and Peña, 1976; Peña et al.,
108 1984), which has been recently dated by Ezquero (2017) to ca. 11.2 Ma. The basin infill shows a
109 gentle roll-over monocline expressed as eastwards tilting ($1-2^\circ$, in average), except for a fringe at
110 the eastern margin where westwards dipping is observed completing a gentle asymmetric
111 syncline. Tilting also affects a planation surface (*Fundamental Erosion Surface, FES*, as defined
112 by Peña et al., 1984) correlative of the uppermost, Middle Pliocene lacustrine deposits of the
113 basin, which have permitted dating the *FES* to 3.5 Ma (Ezquerro, 2017). The *IES* and *FES*
114 planation levels represent useful markers for evaluating offsets across the region (e.g. Rubio and
115 Simón, 2007; Simón et al., 2012).

116 3. Methodology

117 Structural characterization of the eastern, active margin of the Teruel Graben has been
118 mainly achieved by geological mapping, based on field survey and analysis of aerial images

119 (stereoscopic aerial photographs at 1:18,000 scale; orthorectified satellite imagery at 1:5,000
120 scale). Also 5 m grid Digital Elevation Models (DEM) have been used for identifying and
121 drawing traces of some faults with morphological expression.

122 The *IES* and *FES* planation surfaces, as well as their correlative stratigraphical levels
123 have been used as composite, morpho-sedimentary markers for estimating fault throws since
124 the beginning of Teruel Basin development (Tortonian; 11.2 Ma) to Present. Their altitudes
125 have been recently obtained by Ezquerro (2017) from aerial photographs, field surveys and
126 geological cross-sections. Where such markers are directly observable (e.g., *IES* on top of El
127 Pobo Range and their correlative unconformity at the base of the Neogene succession within
128 the basin) those data have allowed calculating fault throws with a precision of about 10-20 m.
129 Where the position of markers has been reconstructed from cross sections, the uncertainty
130 could increase up to ca. 50 m.

131 The orthorectified satellite imagery has also allowed detailed mapping of the dense
132 fracture network in Mesozoic units, and to a lesser extent in the Neogene infill. The strike and
133 length of the different traces were automatically processed through vectorial analysis of
134 mapped fractures by using the QGIS software. From such data, rose diagrams and frequency
135 histograms (both computing the number of faults and weighted according the fracture length)
136 were constructed.

137 Palaeostress analyses have been carried out from populations of small-scale faults
138 collected at 24 sites, from which 30 deviatoric stress tensors have been obtained. The protocol
139 for obtaining stress tensors from faults with slickenline orientations include (Casas et al.,
140 1990): (i) a first approach by means of the Right Dihedra method (Angelier and Mechler,
141 1977) and the y -R diagram (Simón, 1986); (ii) achieving the optimum stress inversion
142 solution(s), including the stress ratio $R = (\sigma_2 - \sigma_3) / (\sigma_1 - \sigma_3)$, using the method proposed by
143 Etchecopar et al. (1981). Analysis of fault samples without slip lineations has been based on

144 the method proposed by Lisle et al. (2001), already successful in this region (Arlegui et al.,
145 2005, 2006), implemented using the computer package FSA of Celérier (2011).

146 Together with these new palaeostress results, other 61 deviatoric stress tensors inferred at a
147 total of 55 measurement sites all over the northern Teruel Basin have been compiled from
148 previous works, with the purpose of increasing and improving the a palaeostress database to
149 obtain a better picture of the complex Neogene tectonic setting. This task has benefited from an
150 abundant literature (Simón, 1983, 1989; Simón and Paricio, 1988, Cortés, 1999; Arlegui et al.,
151 2005, 2006; Liesa and Simón, 2009; Lafuente, 2011; Liesa, 2011a).

152 **4. Major faults of the northern Teruel Basin**

153 The major faults in the northern Teruel Basin occur along the eastern, N-S trending active
154 margin: El Pobo Fault Zone (EPFZ) and La Hita Fault Zone (LHFZ). Others are intra-basinal
155 faults of diverse orientations and ages, several of them located at the junction with the Jiloca
156 Graben: Tortajada, Peralejos, Concud, Teruel and Valdecebro faults (Fig. 2). In the following,
157 we present the main features of these faults including the estimated total throw since the onset of
158 the Teruel Graben, i.e. the vertical displacement of the *IES* planation level (11.2 Ma), as well as
159 the post-*SEF* (3.5 Ma) throw.

160 The EPFZ represents the boundary of the Teruel Graben at its northern sector. It separates
161 Neogene deposits from Mesozoic rocks of the El Pobo Range, giving rise to a 15 km-long
162 mountain front trending N 175° E in average. In more detail the margin exhibits a zigzag pattern
163 made of NNW-SSE trending, en-échelon arranged segments alternating with shorter N-S to
164 NNE-SSW trending ones (Fig. 2). Individual faults are generally less than 1 km-long. A number
165 of them, both synthetic and antithetic with the half-graben boundary, have been observed in
166 outcrops, showing metre- to decametre-scale offsets. Although scarce, slickenlines and other
167 kinematic indicators show consistent normal movements. The total, post-Serravallian vertical

168 displacement (*IES* marker) on the EPFZ is estimated to reach 1040 m, while that occurred since
169 middle Pliocene time (*FES* marker) is 460-520 m (Fig. 3b). Displacement decreases northwards
170 along the EPFZ (Fig. 3a). Together with the antithetic intrabasinal Orrios Fault, the EPFZ
171 bounds the subsident Escorihuela block where a continuous sedimentary series was deposited up
172 to the Early Pleistocene (Ezquerro et al., 2012a,b; Rodríguez-López et al., 2012; Ezquerro,
173 2017).

174 The N-S trending LHFZ defines the central segment of the Teruel Basin margin; it is
175 expressed in the landscape as an irregular mountain front separating the La Hita block from the
176 Valdecebro depression (Fig. 2). At La Hita block, the *IES* and *FES* planation surfaces have an
177 average altitude of 1640 m and 1500 m, respectively, while Ezquerro (2017) and Simón et al.
178 (2018) locates these markers in the Valdecebro depression at 980 and 1250 m, respectively.
179 Consequently, the total throw of LHFZ is estimated to 660 m, while the post-*FES* throw is about
180 250 m. North of this fault, a gentle monocline probably controlled by a N-S blind fault
181 represented the diffuse basin margin until this was shifted to the Tortajada Fault (Fig. 3c).

182 The Tortajada Fault strikes NNE-SSW, separating the central sector of the Teruel Basin
183 from the intermediate Corbalán block (Fig. 2). It was activated during the middle Turolian (Late
184 Miocene, ca. 6.1 Ma), long after the overall Teruel Graben was set up (Ezquerro, 2017). From
185 the geological cross section (Fig. 3c), its total throw is estimated at 350 m, while the post-*FES*
186 throw approaches 260 m.

187 Towards NNE, a number of discontinuous fault traces (Peralejos Faults) apparently
188 constitute the prolongation of the Tortajada Fault. The NNE-SSW trending, 8.5 km-long
189 Peralejos Fault is made of NE-SW en échelon structures that extend up to obliquely abutting the
190 EPFZ. Differently from the Tortajada Fault, the Peralejos Fault was activated since the onset of
191 the Teruel Basin and therefore shows a higher displacement. From the altitude of *IES* and *FES*
192 planation surfaces observed on the footwall block (1755 and 1560 m, respectively) and their

193 position in the hanging wall block (720 and 1040 m, respectively; Fig. 3b), a total throw (post-
194 *IES*) of ca. 1035 m, and a post-*FES* throw approaching 520 m have been estimated.

195 The Conclud Fault is a NW-SE trending structure, whose recent average slip direction
196 towards SW represents the negative inversion of a previous reverse, fold-related fault (Lafuente
197 *et al.*, 2011). It puts in contact Pleistocene alluvial deposits with Triassic and Jurassic units
198 (western and central sectors), and with Neogene units of the Teruel Basin (southeastern sector),
199 representing a junction structure between the Teruel and Jiloca grabens (Fig. 1). The
200 accumulated net displacement for its overall extensional history (since latest Ruscinian, 3.5 Ma;
201 Ezquerro, 2017) has been previously estimated by Lafuente *et al.* (2014) within the range of 255-
202 300 m (throw = 240-280 m) based on the displacement of the top of the pre-tectonic stratigraphic
203 level.

204 The Teruel Fault is an intra-basinal structure that shows a continuous N170°E trending
205 trace at the northern sector, while branches off southwards into two main fault traces trending N-
206 S and NNW-SSE, respectively (Simón *et al.*, 2017). It has accumulated a throw of ca. 250 m
207 since 3.5 Ma, partially accommodated by bending at surface, with average slip direction towards
208 N275°E of its hanging wall block (Ezquerro, 2017; Simón *et al.*, 2017). The Conclud and Teruel
209 faults make a right-stepping, 1.3-km-wide relay zone, while they show no structural link and
210 behave as kinematically independent structures (Simón *et al.*, 2017).

211 Finally, the Valdecebro Fault separates the Jurassic limestones of the upthrown Corbalán
212 block from Miocene-Pliocene deposits of the Valdecebro depression. It is made of a number of
213 extensional, both synthetic and antithetic ruptures striking E-W to ESE-WNW (Simón *et al.*,
214 2018). It has undergone pure normal movement since Early Pliocene times (3.7 Ma), totalizing a
215 throw of 190 m estimated from vertical offset of *FES* (Ezquerro, 2017; Simón *et al.*, 2018).

216 5. Fracture patterns in Mesozoic and Neogene materials

217 The Mesozoic rocks of the eastern footwall blocks (from north to south, El Pobo Range,
218 Cabigordo, and La Hita), the western basin margin (Palomera Range), and the intrabasinal highs
219 (Santa Ana and Sierra Gorda) show a dense network of faults and fractures (Fig. 4). Fracture
220 length ranges from several tens of metres to 6 km, and most of them (10,686 out of 12,666; 84%)
221 are < 500 m in length. Only 49 fractures (0.4 %) are longer than 2 km. In a first approach, the
222 rose diagram compiling directions of individual fractures (Fig. 5a) shows a wide dispersion,
223 although an absolute maximum oriented NE-SW can be identified. In contrast, major faults
224 (traces longer than 2 km) are distinctly oriented, prevailing those striking N-S and NNE-SSW
225 (Fig. 5b). When the azimuth distribution is weighted according to fault length (Fig. 5c), four
226 main sets can be distinguished: (i) NE-SW (range from 020° to 070°, with two relative maxima at
227 030° and 070°); (ii) E-W to ESE-WNW (090°–130°, with three relative maxima at 090°, 105° and
228 125°); (iii) N-S (170°–010°); and (iv) NNW-SSE (140°–160°). Fracture set (i) is widespread and
229 homogeneously scattered all over the region, although it is denser between the latitudes of Teruel
230 and Peralejos (Fig. 4). Fracture sets (ii), (iii) and (iv) have also been observed in all the sectors,
231 but they are better developed in some specific areas (Fig. 4): the N-S set at the Corbalán and
232 north of Cabigordo blocks, and the NNW-SSE and E-W to WNW sets northwards of the
233 Alfambra latitude (El Pobo, Santa Ana and Palomera range blocks).

234 Faults and fractures in Neogene materials include the large structures creating the basin
235 boundary as well as shorter intra-basinal faults, most of them close to the active margin (Fig. 4).
236 Fracture length ranges from 10 m to 10 km, and most of them (1,782 out of 2,571; 69%) have
237 lengths < 500 m. A total of 76 Neogene fractures (3%, clearly higher than for Mesozoic ones) are
238 > 2 km in length. In this case, the azimuth distribution, accounting both absolute number of
239 fractures (Fig. 5d) and accumulated length (Fig. 5f) shows a clear maximum close to N-S (range
240 340° to 020°), although structures quite homogeneously distributed in the rest of directions also

241 exist. Major faults (traces longer than 2 km) show two additional relative maxima around NE-
242 SW and NW-SE (Fig. 5e). The N-S faults and fractures are mainly located at the eastern active
243 margin, while the rest, especially those oriented NE-SW, are mainly distributed in intrabasinal
244 positions. This fracture pattern differs from that described for Mesozoic materials, which allows
245 inferring the true imprint of the Late Neogene, E-W extensional stress field in contrast with the
246 Mesozoic inheritance, as discussed later.

247 **6. Neogene stress fields**

248 In a first approach, the predominance of nearly N-S striking faults in Neogene materials
249 suggests that they could have been activated under an extensional stress field with σ_3 axes
250 trending about E-W. In more detail, this stress field can be reconstructed using the abundant
251 available regional literature (Simón, 1982, 1983, 1989; Paricio and Simón, 1986; Simón and
252 Paricio, 1988; Cortés, 1999; Liesa, 2000, 2011a; Arlegui et al., 2005, 2006; Lafuente, 2011).
253 Table 1 lists the ensemble of palaeostress results ascribed to the Neogene-Quaternary stress
254 systems from those publications. It includes 55 sites mostly located in basinal Neogene-
255 Quaternary sediments (50 sites), while the others lie in pre-Neogene rocks of the basin margin
256 (Fig. 4). Information for each stress solution includes the number of explained faults, the total
257 number of fault data, the orientation of stress axes and the stress ratio, the uncertainty expressed
258 as average misfit angle between theoretical and measured slickenlines, as well as chronological
259 relationships between stress states. In addition, Table 2 lists the results of the new 24 sites in
260 Neogene deposits within the basin studied by Ezquerro (2017) in his unpublished PhD work; for
261 each site, the stereoplot of fault orientations and stress axes representing the resulting stress
262 state(s) is depicted in Figure 4.

263 We use the overall data for refining the regional stress evolution model during Late
264 Neogene-Quaternary times in the central-northern sector of the Teruel Basin. Only 36 among the

265 ensemble of fault sites contain fault planes with slickenlines, which were analysed following the
266 above mentioned protocol based on *Righth Dihedra*, Etchecopar's and *y-R* methods (Angelier and
267 Mechler, 1977; Etchecopar et al., 1981; Simón, 1986). The remaining sites (43) had meso-scale
268 fault planes showing small offsets but no visible striations, these being analysed using the method
269 proposed by Lisle et al. (2001). While the former sites could provide reliable stress orientations
270 and stress ratios ($R = (\sigma_2 - \sigma_3) / (\sigma_1 - \sigma_3)$), the latter have not allowed acceptable constraint of R
271 values. In the case of the non-striated fault planes studied by Ezquerro (2017), R values provided
272 by the FSA software (Celérier, 2011) are included in Table 2, but their reliability is also weak.

273 The ensemble of palaeostress results on the Teruel Basin includes 58 complete deviatoric
274 stress tensors, and 33 stress solutions for which the R ratio is unknown (Fig. 6). In almost all
275 sites, the inferred σ_1 axis is nearly vertical, in agreement with the extensional character of the
276 Neogene regional stress field. Only four stress tensors have horizontal σ_1 axis and, except for
277 one, subvertical σ_2 axis, i.e. mainly representing strike-slip stress regimes. Accordingly, only the
278 trend of the main principal horizontal axis (σ_3 in extensional regime and σ_1 in compressional or
279 strike-slip ones) was compiled in Tables 1 and 2.

280 Several fault surfaces have two (exceptionally three) different striae generations. In
281 general, the first set shows lower pitch than the second one, the latter being close to 90° and
282 always exhibiting normal kinematics. Such cross-cut relationships between striae sets, together
283 with the early or later deformational character of faulting, and the stress orientation in relation
284 with bed attitude (pre- and post-tilting stress state; e.g. Simón, 1982, 1996; Angelier et al., 1985;
285 Liesa and Simón, 2009) have been used for relatively dating palaeostress states in some sites
286 (e.g. P6, P17, P19, P31, and P38 in Table 1, and sites 3, 9, 14, 15, and 23 in Table 2). Such
287 chronological constraints are included in Tables 1 and 2 and graphically displayed (arrows) in
288 Figure 6.

289 The four datasets characterized by a horizontal σ_1 have directions NNE-SSW and NNW-
290 SSE to N-S (labelled as A and B, respectively, in Fig. 6a). Chronological constraints indicate that
291 they likely acted prior to the extensional stress states, and that the NNE-SSW direction was prior
292 to the N-S one (see arrows associated to sites 23 and P31 in Fig. 6a).

293 Concerning the direction of horizontal σ_3 axes in a purely tensile regime ($R>1$), the
294 synthetic y-R diagram (Fig. 6a) and histograms (Fig. 6b,c) show their distribution for stress
295 states affecting the Late Miocene-Quaternary sedimentary succession. The overall results show
296 the predominance of σ_3 axes flipping around the E-W direction, although two maxima can be
297 distinguished: an absolute maximum close to ENE-WSW (azimuth 055°-075°; label 1 in Fig. 6b),
298 and a second, relative maximum close to E-W (085°-100°; label 2 in Fig. 6b). Other relative
299 maxima can be observed around the directions NNE-SSW to NE-SW (030°-040°), NW-SE
300 (120°-130°), and N-S (350°-000°) (labels 3, 4 and 5, respectively, in Fig. 6b).

301 If we consider the age of the deposits where such stress systems have been recorded (Fig.
302 6c), E-W σ_3 directions are dominant during Late Miocene-Early Pliocene (Turolian-Ruscinian),
303 while ENE-WSW σ_3 directions are mainly recorded in Villafranchian-Pleistocene sediments
304 (where the E-W extension is not represented). The other directions (maxima 3, 4 and 5) appear
305 all along the stratigraphical series.

306 With respect to the spatial distribution of inferred extensional directions, the ENE-WSW
307 (1) and E-W (2) are recorded all along the basin and related to different structural settings (Fig.
308 4). The other extensional directions (3, 4 and 5) are recorded at few localities trending either
309 parallel or perpendicular to major structures. As an example, the NNE-SSW to NE-SW (3) and
310 NW-SE (4) mainly appear near the NW-SE Conclud Fault or the NE-SW Tortajada Fault. This
311 suggests that they represent local deflections of stress trajectories, as those modelized by e.g.,
312 Simón et al. (1988) and Katternhorn et al. (2000), and identified by Simón (1989) and Arlegui et
313 al. (2006) in this region.

314 Apart from the older compressional and strike-slip episodes, the Neogene stress field
315 evolution has been therefore characterized from the whole analysis of the distribution of
316 azimuths and R values of extensional stress states affecting the sedimentary sequence (Fig. 6),
317 mesostructural evidence on their relative age (Tables 1, 2), and the heterogeneous spatial
318 distribution of stress directions attributed to stress deflection (Fig. 4). The results suggest the
319 occurrence of two major extensional stress episodes: (i) the first episode (Vallesian–Ruscinian or
320 Tortonian–Zanclean in age) is characterized by a triaxial stress regime with well-defined σ_3 axes
321 trending close to E-W; (ii) the second one (since early Villafranchian or Piacenzian) is
322 characterized by almost radial extensional regime (σ_1 vertical, $\sigma_2 \approx \sigma_3$; very high R values).
323 Although multiple σ_3 maxima are assigned to this second episode from the available dataset (as a
324 consequence of stress deflection phenomena; see section 7.2), the overall regional results suggest
325 that the ENE-WSW trending σ_3 axes represent its primary or remote stress system (Simón 1989;
326 Arlegui et al., 2005). The chronological distribution of stress solutions depicted in Figure 6c also
327 corroborates that the ENE-WSW extension direction prevails since Villafranchian time.

328 7. Discussion

329 7.1. Discerning structural inheritance

330 As a first approach, the differences observed between fracture patterns described for
331 Mesozoic and Neogene rocks suggest: (i) the essential structural imprint of the Late Neogene, E-
332 W and ENE-WSW oriented extensional stress systems is associated with the N-S trending fault
333 set; (ii) the structural inheritance from ancient tectonic phases is mainly represented by NE-SW
334 and E-W to ESE-WNW trending faults and fractures, and also probably by NNW-SSE ones.

335 Large (> 20 km) NNW-SSE trending, nearly vertical faults appear eastwards from the
336 study area (e.g. Miravete, Alpeñés and Ababuj faults), most of them likely originated during

337 Variscan or late-Variscan tectonic phases (Soria, 1997; Liesa et al., 2006). These faults, together
338 with newly formed, NE-SW to ENE-WSW striking, low angle listric faults, controlled the
339 structural development and sedimentation of the Galve sub-basin during the Late Jurassic-Early
340 Cretaceous rifting phase affecting eastern Iberia (Soria, 1997; Soria et al., 2000; Capote et al.,
341 2002; Liesa et al., 2004, 2006; Navarrete et al., 2013). This rifting stage was responsible for the
342 development of a dense fracture network at different scales, mainly affecting the prerift Jurassic
343 carbonate rocks (as in the El Pobo Range) but also the synrift sediments of the Cretaceous
344 Maestrazgo Basin (Liesa, 1992-1995, 1993, 2000, 2011a; Liesa and Simón, 1994; Antolín-
345 Tomás et al., 2007). Based on the spatial distribution, changes in orientation, relative dimensions
346 and cross-cut relationships of major faults, small-scale faults and joints in the El Pobo Range,
347 Liesa (2000, 2011a) stated that they are arranged in two fractures systems. Each system consists
348 of two orthogonal sets: the older sets are oriented NW-SE and NE-SW, while the younger ones
349 trend N-S and E-W, respectively. A similar fracture network is expected to occur at the Jurassic
350 basement of the Neogene Teruel Basin. During Palaeogene and Early Neogene times, most of
351 those major faults underwent positive inversion under compressional stress fields linked to the
352 Alpine orogeny; as a result, they controlled the position, style and evolution of most
353 contractional structures (Simón et al., 1998; Liesa and Simón, 2004, 2011; Liesa et al., 2004).

354 In this way, the Neogene extension acted on an extremely heterogeneous Mesozoic-
355 Cenozoic sedimentary cover, densely fractured during multiple tectonic episodes. Taking into
356 account the stress regime and stress orientations characterizing each rifting episode, it could be
357 deduced that: (i) the earlier, Late Miocene to Early Pliocene triaxial extension was the main
358 responsible for reactivated or newly created faults, clustered around N-S trend; (ii) the later, Late
359 Pliocene to Quaternary 'multidirectional' extension was able to reactivate such N-S trending
360 faults as well as most previous, inherited fault sets of varying orientations.

361 A clear example of reactivation of a previous contractional structure is the case of the NW-
362 SE Conclud fault. This normal fault represents the southernmost structure of the Jiloca Basin
363 (Fig. 1), which formed during the Late Pliocene and cut the sedimentary infill of the previous N-
364 S Teruel Basin (e.g. Moissenet, 1983; Simón, 1983). This fault follows the near vertical to
365 overturned limb of an NW-SE anticline with a Triassic core. This relation suggests that the
366 Conclud normal fault could represent the negative inversion of a reverse fault that developed
367 (with an associated propagation fold) during the Palaeogene compressional stage. This
368 interpretation was verified by Lafuente (2011) and Lafuente et al. (2011) when evinced (i) a
369 hectometre-scale klippe of Triassic rocks over Jurassic ones at the central part of the fault trace,
370 and (ii) a ductile shear band, contiguous and subparallel to the present-day normal fault,
371 developed in Triassic lutites with an internal S-C fabric indicating a reverse-dextral movement.

372 The Teruel Basin itself could also represent the reactivation of a major NNE-SSW
373 basement structure since it separates two sectors where the compressional structures show quite
374 different strikes. The Jurassic intrabasinal highs and the western sectors of the basin show folds
375 mainly trending NW-SE (Godoy et al., 1993a), while main folds in the eastern sector (the El
376 Pobo Range and eastwards) trend NNW-SSE and have ENE-WSW superposed folds (Simón et
377 al., 1998; Liesa, 2000, 2011b; Liesa et al., 2004). Such major crustal structure has been also
378 proposed as responsible for deviating the σ_1 stress trajectories of the *Iberian* and *Betic* intraplate
379 compressional stress fields during the Alpine Orogeny (Liesa, 2000; Capote et al., 2002; Liesa
380 and Simón, 2007, 2009).

381 7.2 *The dynamic framework: strain/stress partitioning within the Late Neogene-Quaternary* 382 *stress field*

383 The palaeostress results revealed here are consistent with the evolutionary model proposed
384 by Simón (1982, 1983, 1989), in which two rift episodes control the development of Neogene

385 basins in the eastern Iberian Chain. During the first episode, Late Miocene in age, the NNE-SSW
386 trending Teruel and Maestrazgo grabens developed under a dominant E-W to ESE-WNW
387 extension (Simón, 1982, 1986, 1989; Cortés, 1999; Capote et al., 2002; Liesa, 2011a). The
388 second rift episode has been linked to crustal doming taking place in the eastern Iberian Chain
389 during Late Neogene-Quaternary times (Simón, 1982, 1989). This hypothesis is supported by
390 geophysical evidence on a negative density anomaly in the upper mantle of this region
391 (Piromallo and Morelli, 2003; Boschi et al., 2010), which could have induced a positive dynamic
392 topography of several hundred metres (Scotti et al., 2014). The resulting stress field is
393 characterized by nearly ‘multidirectional’ tension with primary σ_3 trajectories trending ENE-
394 WSW, giving rise to development of the NNW-SSE trending Jiloca gaben, the reactivation of
395 most of the previous extensional margins, and pervasive deformation of the *Fundamental*
396 *Erosion Surface* (Simón, 1982, 1989; Capote et al., 2002; Arlegui et al., 2005, 2006; Liesa,
397 2011a).

398 The regional stress fields active during both rift episodes show spatial heterogeneities.
399 Within the overall available palaeostress database, secondary relative maxima of σ_3 axes at
400 azimuths 350°–000° (labelled as 5 in Fig. 6), 030°–040° (3), and 120°–130° (4) should be
401 interpreted in terms of stress deflections and stress swaps induced by major faults, mainly in the
402 second, near multidirectional extensional episode. Such interpretation is based on the parallelism
403 or orthogonality observed between some of these σ_3 directions (mainly for 350°–000° and 030°–
404 040° ones) and some of the major faults (e.g. sites P33 and P36 with respect to EPFZ; sites 10,
405 11, 17-20 and 21 with respect to Peralejos and Tortajada faults; or sites P19, P20, P28, P30, P42
406 and 21 with respect to the Conclud Fault; Fig. 4). Minor-order stress heterogeneities are frequent
407 within ‘radial’ or ‘multidirectional’ tension stress fields. First, trajectories of the minimum stress
408 axis (σ_3) undergo frequent deflections, veering to become either parallel or perpendicular to
409 NNW-SSE and NNE-SSW major faults, which follow the numerical models of stress deflections

410 (e.g. Simón et al., 1988; Kattenhorn et al., 2000). A progressive variation of the shape of stress
411 ellipsoids, from near-multidirectional to triaxial tension, frequently accompanies such deflection
412 as approaching active faults (Arlegui et al., 2006). Second, swap events between σ_2 and σ_3 axes
413 are also common phenomena in the region (Simón et al., 1988; Simón, 1989), which can explain
414 the occurrence of both joint sets and conjugate normal fault systems striking at right angles to the
415 master faults.

416 Concerning the timing of stress systems, the results summarised in Figure 6c suggest that
417 the transition between stress systems associated to both rift episodes possibly occurred close to
418 the Ruscinian-Villafranchian boundary. Nevertheless, both E-W to ESE-WNW, and ENE-WSW
419 extension directions have been recorded within the Miocene-Pliocene series. This suggests that
420 they do not strictly represent two successive tectonic phases, but separation of the extensional
421 stress field into two stress systems, with S_{Hmax} (maximum horizontal stress axis) nearly parallel
422 to the trends of the Teruel and Jiloca grabens, respectively. Moreover, such S_{Hmax} directions
423 replicate the main far-field stresses acting during the Neogene-Quaternary in eastern Spain: the
424 intraplate NNW-SSE compression produced by Africa-Iberia convergence, and the WNW-ESE
425 extension induced by rifting at the Valencia trough (Simón, 1989; Herraiz et al., 2000; Capote et
426 al., 2002; Arlegui et al., 2005). Such stress setting has been defined by Simón *et al.* (2008) as
427 *stress partitioning*, i.e. ‘time dissociation’ of the overall stress field into distinct genetic stress
428 systems similar to that described in the Italian Alps as *Twist Tectonics* by Caputo et al. (2010).
429 In accordance with the above explained processes, progressive deformation occurs in the form of
430 a non-linear succession of fracture episodes; each of them is controlled by stress boundary
431 (‘Andersonian’) conditions, while the ensemble of them finally accommodates triaxial bulk
432 deformation of the rock body (Simón et al., 2008).

433 Partitioning of the Neogene-Quaternary stress/strain field in Eastern Iberia is a
434 consequence of both the complex tectonic framework and the influence of inherited structures.

435 The WNW-ESE extension active by the Late Miocene is linked to rifting at the Valencia Trough
436 (Simón, 1982), but it is also coaxial with the later *Pyrenean compression* (maximum horizontal
437 stress, S_{Hmax} trending NNE-SSW), as defined by Liesa (2000), Capote et al. (2002) and Liesa and
438 Simón (2007, 2009). The WSW-ENE extension that dominates during Late Pliocene and
439 Quaternary times reveals the presence of NNW-SSE trending S_{Hmax} trajectories (maximum
440 horizontal stress) controlled by the recent Iberia-Africa convergence (Simón, 1989; Herraiz et
441 al., 2000; Arlegui et al., 2005). Both tectonic mechanisms coexist during the whole Neogene and
442 Quaternary, and both extension directions, WNW-ESE and WSW-ENE, are recurrently recorded
443 during this time lapse indeed (Cortés et al., 1996; Arlegui and Simón, 2000; Arlegui et al., 2005).
444 Episodic ‘inhibition’ of one of them owing to stress release subsequent to fault movement may
445 allow the second one to be manifested (Simón et al., 2008). They can be therefore recorded as
446 separate stress states in different areas within the whole region (spatial stress partitioning) as well
447 as in different time windows within the whole tectonic period (temporal stress partitioning).

448 Such dissociation of stress systems was facilitated by the existence of diverse inherited
449 fault sets. Once these faults were progressively propagated, the successive stress systems
450 selectively activated those favourably oriented. Slip on master structures controlling Neogene
451 grabens probably accommodated most of the total deformation, i.e. NNE-SSW faults driven by
452 rifting at the Valencia Trough, and NW-SE to NNW-SSE faults born as contractional structures
453 during Palaeogene orogeny, then inverted during Neogene rifting. But the whole region
454 (specifically, the El Pobo Range and Alfambra depression) shows other multiple fault sets (most
455 of them inherited from Mesozoic extensional episodes; Liesa, 2000, 2011b). The ensemble of
456 them provided the best possible conditions for stress-strain partitioning, mainly during the later
457 ‘multidirectional’ extensional episode.

458 7.3. *The resulting zigzag basin margin and intrabasinal deformation*

459 As a result of fault linkage within the described structural and dynamic ascenario, the
460 eastern margin of the northern Teruel Basin acquired a zigzag arrangement at the same time as
461 the intrabasinal structure was getting more and more complex. In homogeneous and isotropic
462 materials, evolution of relay zones up to accomplish linkage uses to follow its own kinematic
463 rules, essentially controlled by the relationship between geometry, transport direction and
464 interaction of master faults (e.g. Cartwright et al., 1995; Gupta and Scholz, 2000). By contrast, in
465 more complex tectonic settings inherited structures and their response to stress are the main
466 controls of fault linkage and margin arrangement, as well as of intrabasinal deformation.

467 In the northernmost sector of the Teruel Basin, the orientation of faults that control the
468 alternating N-S to NNE-SSW, and NNW-SSE trending segments (Fig. 7) coincide with the two
469 main directions of large-scale faults ($L > 2$ km) cutting Mesozoic rocks. Moreover, both fault
470 directions are nearly orthogonal to the σ_3 trajectories of the prevailing stress systems: E-W to
471 ESE-WNW (earlier extensional episode), and ENE-WSW (later extensional episode). Therefore,
472 in this case, a dynamic scenario based on successive episodes of reactivation of pre-existing
473 faults under favourable stress conditions provides a more feasible explanation for fault linkage
474 than a scenario only controlled by fault interaction. Based on tectono-sedimentary relationships at
475 the short segments of the northernmost, zigzag arranged, EPFZ, Ezquerro (2017) has
476 demonstrated how NNW-SSE trending segments developed prior to the N-S to NNE-SSW
477 trending ones. Such sequence of fault episodes in those distinctly oriented segments is the
478 opposite to the regional rifting sequence, and are constrained to the second rift episode
479 (Ruscinian-Villafranchian; Ezquerro, 2017). This suggests that we are not properly dealing with
480 successive stress episodes, but with a typical case of space-time stress partitioning (Caputo,
481 2005). Their interpretation is that NNW-SSE striking faults were firstly activated under ENE-
482 WSW extension characterizing the Late Pliocene stress field. Subsequently, local perturbation

483 related to interaction between neighbouring faults produced a slight change of the stress
484 trajectories, the σ_3 direction flipping to E-W or ESE-WNW and thus triggering activation of
485 NNE-SSW segments. In this way, two successive stress episodes, representing both time and
486 space partitioning of the regional stress field (Simon et al., 2008), have resulted in a somewhat
487 orthorombic or ‘biconjugate’ fault system that accommodates three-dimensional bulk
488 deformation (Reches, 1978; Reches and Dieterich, 1983; Crider and Pollard, 1998).

489 On the basis of the presented data, a similar situation can be envisaged for the ensemble of
490 the central-northern sector of the Neogene Teruel Basin (Fig. 8). Accordingly, we propose a
491 scenario in which the evolving extensional stress system was able to gradually activate major
492 basement structures of variable direction inherited from previous deformational stages, then
493 controlling the structure and evolution of both the margin and central parts of the basin. Timing
494 and amplitude of fault displacements are constrained from throws measured on the successive
495 sedimentary units as well as on the planation surfaces, *IES* (11.4 Ma) and *FES* (3.5 Ma). The
496 combined use of such sedimentary and geomorphological markers allow reconstructing the
497 timing of both intrabasinal and boundary master faults. Roughly N-S to NNE-SSW trending,
498 eastern border faults (e.g. the EPFZ (south sector) and LHFZ and the Peralejos Faults) frequently
499 record significant displacements during the Late Miocene (post-*IES* to pre-*FES*), as much as in
500 recentmost times (post-*FES*). Intrabasinal faults of variable direction, however, show a much
501 lower (Tortajada, Teruel, and Valdecebro faults) or null (Concud fault) displacement in the first
502 stage, whereas they undergo higher activity in more recent times.

503 Accordingly, Figure 8 shows an evolutionary model in two stages. The overall Teruel
504 Graben was onset at the beginning of the Late Miocene (~ 11.2 Ma), when the N-S fault zones of
505 its eastern margin (La Hita and El Pobo) were activated within an E-W to ESE-WSW triaxial
506 extension. The LHFZ likely continued northwards as a blind structure, as suggested by the
507 aligned N-S trending monocline observed at the Cabigordo block (Fig. 3c) and the high vertical

508 offset pre-*FES* associated to it (Ezquerro, 2017). In addition, the Peralejos Fault interposed
509 between the two major fault zones also recorded high displacements. At this stage, this NE-SW
510 trending structure represented a long linking zone between EPFZ and LHFZ, where NNE-SSW
511 segments were reactivated to form a NE-SW trending right-stepping relay setting. During the
512 Late Pliocene (~ 3.5 Ma), when the remote extensional stress regime became almost radial ($\sigma_2 \approx$
513 σ_3) though with a prevailing ENE-WSW tensile direction, the former structures remained active
514 while other faults of variable direction were reactivated mainly in intrabasinal sector. Northward
515 propagation of the EPFZ also occurred in this second stage, after development of the *FES*
516 planation level (Ezquerro, 2017). The transition between both stages likely occurred in a
517 progressive manner, as suggested by the onset of the NNE-SSW Tortajada Fault during the
518 middle Turolian (Late Miocene, ca. 6.1 Ma). In its hangingwall, sediments of this age have
519 reworked clasts of Neogene conglomerates sourced at the Corbalán footwall block (Ezquerro,
520 2017).

521 The above described intrabasinal and bordering fault network of the Teruel Basin is more
522 complex than those normally displayed in other intracontinental rift basins (e.g. Basin and Range
523 in USA or East African rift system), where more linear structures (rift valleys) are present. As it
524 has been shown, such complex structure of the central-northern Teruel Basin was clearly
525 controlled by both the variable orientation of inherited structures and the evolving, Late Miocene
526 to Quaternary regional stress field. Active processes in central-eastern Iberia changed in time due
527 to the complex plate kinematics of the relatively small Iberian plate and the neighbouring Europe
528 and Africa major plates. Intraplate deformation was strongly influenced by the evolving
529 interaction between the stress systems mainly transmitted from the plate boundaries, i.e. the
530 remained NNE-SSW Iberia-Europe convergence, the NNW-SSE Africa-Iberia convergence, the
531 E-W active extension in the eastern Valencia Trough, and the crustal doming process during
532 Pliocene-Quaternary times.

533 8. Conclusions

534 Two distinct episodes can be distinguished during the evolution of the Teruel Basin: (i) an
535 earlier episode (Late Miocene-Early Pliocene in age) characterized by triaxial extension with σ_3
536 trajectories close to E-W, and (ii) a later episode (Late Pliocene-Quaternary) with prevailing
537 ENE-WSW trending σ_3 trajectories though characterized by an almost radial extensional regime.

538 The earlier stress episode was responsible for the onset of the northern Teruel half-graben
539 and propagation of a major, N-S trending set of newly formed faults. Nevertheless, a dense
540 network made of NNE-SSW and NNW-SSE striking segments, mostly consisting of inherited
541 Mesozoic fractures, also contributed to the development of the eastern basin margin. Mainly at
542 its northernmost sector, early linkage through narrow fault relay zones enabled prompt
543 development of a zigzag arrangement (Fig. 7). These faults were selectively reactivated under
544 the E-W extensional stress field (a process usually easier than the formation of new faults), and
545 remain as well active during the second stress episode.

546 At the central sector of the basin, activation of faults of other diverse orientations (Concud,
547 NW-SE; Tortajada, NE-SW; Valdecebro, E-W), resulted in a more complex structural network.
548 Such activations also occurred during the second stress episode, during which 'radial'
549 extensional deformation should be necessarily accommodated by a variety of fault sets.

550 Both structural inheritance and deformational processes (especially the remote and
551 driving stress systems) appear as first-order factors in the resulting structure and evolution of rift
552 basins because they ultimately control whether inherited or newly-formed structures will
553 developed.

554 Acknowledgements

555 We wish to acknowledge the thorough reviews and valuable comments of Kieran F.
556 Mulchrone and Riccardo Caputo. We want to extend our appreciation to Editor Joao Hippertt for
557 taking the time and necessary effort to help in the improvement of this work. The research has
558 been financed by projects CGL2012-35662 of Spanish Ministerio de Economía y
559 Competitividad-FEDER, and UZ2017-CIE-01 of Universidad de Zaragoza. This work is a
560 contribution of the *Geotransfer* research group, co-financed by the Aragón Government and the
561 PO FEDER Aragón 2014-2020.

562 **References**

- 563 Alcalá, L., Alonso-Zarza, A.M., Álvarez, M.A., Azanza, B., Calvo, J.P., Cañaveras, J.C., van
564 Dam, J.A., Garcés, M., Krijgsman, W., van der Meulen, A.J., Morales, J., Peláez, P., Pérez-
565 González, A., Sánchez, S., Sancho, R., Sanz, E., 2000. El registro sedimentario y faunístico de
566 las cuencas de Calatayud-Daroca y Teruel. Evolución paleoambiental y paleoclimática
567 durante el Neógeno. *Revista de la Sociedad Geológica de España* 13, 323-343.
- 568 Alonso-Zarza, A.M., Calvo, J.P., 2000. Palustrine sedimentation in an episodically subsiding
569 basin: the Miocene of the Northern Teruel Graben (Spain). *Palaeogeography,*
570 *Palaeoclimatology, Palaeoecology* 160, 1-21.
- 571 Álvaro, M., Capote, R., Vegas, R., 1979. Un modelo de evolución geotectónica para la Cadena
572 Celtibérica. *Acta Geológica Hispánica* 14, 172-177.
- 573 Angelier, J., Mechler, P., 1977. Sur une méthode graphique de recherche des contraintes
574 principales également utilisable en tectonique et en séismologie: la méthode des dièdres
575 droits. *Bulletin de la Societé Géologique de France* 19, 1309–1318.
- 576 Angelier, J., Colleta, B., Anderson, R.E., 1985. Neogene paleostress changes in the Basin and
577 Range: A case study at Hoover Dam, Nevada-Arizona. *Geological Society of America*

- 578 Bulletin 96, 347-361.
- 579 Antolín-Tomás, B., Liesa, C.L., Casas, A.M., Gil-Peña, I., 2007. Geometry of fracturing linked
580 to extension and basin formation in the Maestrazgo basin (Eastern Iberian Chain, Spain).
581 Revista de la Sociedad Geológica de España 20, 351-365.
- 582 Arlegui, L.E., Simón, J.L., 2000. Fracturación y campos de esfuerzos en el Cuaternario del sector
583 central de la Cuenca del Ebro (NE España). Cuaternario y Geomorfología 14, 11-20.
- 584 Arlegui, L.E., Simón, J.L., Lisle, R.J., Orife, T., 2005. Late Pliocene-Pleistocene stress field in
585 the Teruel and Jiloca grabens (eastern Spain): contribution of a new method of stress
586 inversion. Journal of Structural Geology 27, 693-705.
- 587 Arlegui, L.E., Simón, J.L., Lisle, R.J., Orife, T., 2006. Analysis of non-striated faults in a recent
588 extensional setting: the Plio-Pleistocene Conclud fault (Jiloca graben, eastern Spain). Journal
589 of Structural Geology 28, 1019-1027.
- 590 Boschi, L., Faccenna, C., Becker, T. W., 2010. Mantle structure and dynamic topography in the
591 Mediterranean Basin. Geophysical Research Letters 37, doi: 10.1029/2010GL045001.
- 592 Bott, M.H.P., 1959. The mechanics of oblique slip faulting. Geological Magazine 96, 109-117.
- 593 Capote, R., Muñoz, J.A., Simón, J.L., Liesa, C.L., Arlegui, L.E., 2002. Alpine tectonics I: The
594 Alpine system north of the Betic Cordillera. In: Gibbons, W., Moreno, T. (Eds.) Geology of
595 Spain, The Geological Society, London. 367-400.
- 596 Caputo, R., 2005. Stress variability and brittle tectonic structures. Earth Science Reviews 70,
597 103-127.
- 598 Caputo, R., Poli, M.E., Zanferrari, A., 2010. Neogene–Quaternary tectonic stratigraphy of the
599 eastern Southern Alps, NE Italy. Journal of Structural Geology 32, 1009–1027.

- 600 Cartwright, J.A., Trudgill, B.D., Mansfield, C.S., 1995. Fault growth by segment linkage: an
601 explanation for scatter in maximum displacement and trace length data from the Canyonlands
602 Graben of S.E. Utah. *Journal of Structural Geology* 17, 1319–1326.
- 603 Casas, A.M., Gil, I., Simón, J.L., 1990. Los métodos de análisis de paleoesfuerzos a partir de
604 poblaciones de fallas: sistemática y técnicas de aplicación. *Estudios Geológicos* 46, 385-398.
- 605 Celérier, B., 2011. FSA: Fault, Stress Analysis software, version 33.7. [http://www.pages-perso-](http://www.pages-perso-bernard-celerier.univ-montp2.fr/software/dcmt/fsa/fsa.html)
606 [bernard-celerier.univ-montp2.fr/software/dcmt/fsa/fsa.html](http://www.pages-perso-bernard-celerier.univ-montp2.fr/software/dcmt/fsa/fsa.html)
- 607 Cortés, A.L., 1999. Evolución tectónica reciente de la Cordillera Ibérica, Cuenca del Ebro y
608 Pirineo centro-occidental. Ph.D. Thesis. University of Zaragoza, Zaragoza, pp. 409.
- 609 Cortés, A.L., Liesa, C.L., Simón, J.L., Casas, A.M., Maestro, A., Arlegui, L.E., 1996. El campo
610 de esfuerzos compresivo neógeno en el NE de la Península Ibérica. *Geogaceta* 20, 806-809.
- 611 Crider, J.G., Pollard, D.D., 1998. Fault linkage: Three dimensional mechanical interaction
612 between echelon normal faults. *Journal of Geophysical Research* 103, 24 373–24 324
- 613 Etchecopar, A., Vasseur, G., Daignières, M., 1981. An inverse problem in microtectonics for the
614 determination of stress tensors from fault striation analysis. *Journal of Structural Geology* 3,
615 51–65.
- 616 Ezquerro, L., 2017. El sector norte de la cuenca neógena de Teruel: tectónica, clima y
617 sedimentación. Ph.D. Thesis, University of Zaragoza, Zaragoza, pp. 494 p.
- 618 Ezquerro, L., Luzón, M.A., Liesa, C.L., Simón, J.L., 2012a. Evolución megasecuencial del
619 relleno mio-plioceno del sector norte de la cuenca de Teruel: interacciones entre tectónica y
620 sedimentación. In: Fernández, L.P., Fernández, A., Cuesta, A., Bahamonde, J.R. (Eds.)
621 *GeoTemas* 13, Resúmenes extendidos del VIII Congreso Geológico de España, 171-174.

- 622 Ezquerro, L., Lafuente, P., Pesquero, M^a.D., Alcalá, L., Arlegui, L.E., Liesa, C.L., Luque, L.,
623 Rodríguez-Pascua, M.A., Simón, J.L., 2012b. Una cubeta endorreica residual plio-pleistocena
624 en la zona de relevo entre las fallas de Concud y Teruel: implicaciones paleogeográficas.
625 *Revista de la Sociedad Geológica de España* 25, 157-175.
- 626 Godoy, A., Olivé, A., Moissenet, E., Gutiérrez Elorza, M., Aguilar, M.J., Ramírez, J.I.,
627 Aragonés, E., Giner, J., Portero, J.M., 1983a. Mapa Geológico de España 1:50.000, hoja n°
628 542 (Alfambra). IGME, Madrid.
- 629 Godoy, A., Ramírez, J.I., Olivé, A., Moissenet, E., Aznar, J.M., Aragonés, E., Aguilar, M.J.,
630 Ramírez del Pozo, J., Leal, M.C., Jerez Mir, L., Adrover, R., Goy, A., Comas, M.J., Alberdi,
631 M.T., Giner, J., Gutiérrez Elorza, M., Portero, J.M., Gabaldón, V., 1983b. Mapa Geológico de
632 España 1:50.000, hoja n° XXX (Teruel). IGME, Madrid.
- 633 Gupta, S., Scholz, C.H., 2000. A model of normal fault interaction based on observations and
634 theory. *J. Struct. Geol.* 22, 865-880.
- 635 Gutiérrez, M., Peña, J.L., 1976. Glacis y terrazas en el curso medio del río Alfambra (provincia
636 de Teruel). *Boletín Geológico y Minero* 87, 561-570.
- 637 Herraíz, M., De Vicente, G., Lindo, R., Giner, J., Simón, J.L., González, J.M., Vadillo, O.,
638 Rodríguez, M.A., Cicuéndez, J.I., Casas, A., Rincón, P., Cortés, A.L., Lucini, M., 2000. The
639 recent (Upper Miocene to Quaternary) and present tectonics stress distributions in the Iberian
640 Peninsula. *Tectonics* 19, 762-786.
- 641 Homberg, C., Hu, J.C., Angelier, J., Bergerat, F., Lacombe, O., 1997. Characterization of stress
642 perturbations near major fault zones: Insights from 2-D distinct-element numerical modelling
643 and field studies (Jura mountains). *Journal of Structural Geology* 19, 703-718.

- 644 Katterhorn, S.A., Aydin, A., Pollard, D.D., 2000. Joints at high angles to normal fault strike: an
645 explanation using 3-D numerical models of fault-perturbed stress fields. *Journal of Structural*
646 *Geology* 22, 1-23.
- 647 Lafuente, P., 2011. Tectónica activa y paleosismicidad de la falla de Conclud (Cordillera Ibérica
648 central). Ph.D. Thesis. University of Zaragoza, Zaragoza.
- 649 Lafuente, P., Arlegui, L.E., Liesa, C.L., Simón, J.L., 2011. Paleoseismological analysis of an
650 intraplate extensional structure: the Conclud fault (Iberian Chain, Spain). *International*
651 *Journal of Earth Sciences* 100, 1713–1732.
- 652 Larroque, J.M., Laurent, P., 1988. Evolution of the stress field pattern in the south of the Rhine
653 Graben from the Eocene to the present. *Tectonophysics* 148, 41-58.
- 654 Liesa, C.L., 1992-1995. Estudio de la fracturación de las rocas a distintas escalas en campos de
655 esfuerzos complejos en Mosqueruela y la Sierra de Camarena (provincia de Teruel). Teruel
656 83-84, 31-80.
- 657 Liesa, C.L., 1993. Análisis de la deformación frágil en las áreas de Mosqueruela y La Puebla de
658 Valverde (Teruel): fases tectónicas y perturbaciones de esfuerzos. Unpublished Tesis de
659 Licenciatura, Univ. of Zaragoza, Zaragoza, pp. 98.
- 660 Liesa, C.L., 2000. Fracturación y campos de esfuerzos compresivos alpinos en la Cordillera
661 Ibérica y el NE peninsular. Ph.D. Thesis. University of Zaragoza, Zaragoza, pp. 760.
- 662 Liesa, C.L., 2011a. Fracturación extensional cretácica en la Sierra del Pobo (Cordillera Ibérica,
663 España). *Revista de la Sociedad Geológica de España* 24, 31-48.
- 664 Liesa, C.L. 2011b. Evolución de campos de esfuerzos en la Sierra del Pobo (Cordillera Ibérica,
665 España). *Revista de la Sociedad Geológica de España* 24, 49-68.

- 666 Liesa, C.L., Simón, J.L., 1994. Fracturación a distintas escalas y campos de esfuerzos durante la
667 tectogénesis alpina en el área de Mosqueruela (Teruel). *Estudios Geológicos* 50, 47-57.
- 668 Liesa, C.L., Simón, J.L., 2004. Modelos de inversión positiva en sistemas de fallas en graderío:
669 los márgenes de las cuencas extensionales cretácicas en la Cordillera Ibérica centro-oriental.
670 *Geotemas* 6, 229-232.
- 671 Liesa C.L., Simón, J.L., 2007. A probabilistic approach for identifying independent remote
672 compressions: The case of the Iberian Chain (NE Spain). *Mathematical Geology* 39, 337-348.
- 673 Liesa, C.L., Simón, J.L., 2009. Evolution of intraplate stress fields under multiple compressions:
674 The case of the Iberian Chain (NE Spain). *Tectonophysics* 474, 144-159.
- 675 Liesa, C.L.; Casas, A.M.; Soria, A.R.; Simón, J.L.; Meléndez, A. (2004) Estructura extensional
676 cretácica e inversión terciaria en la región de Aliaga-Montalbán. In: Colombo, F., Liesa, C.L.,
677 Meléndez, A., Pocoví, A., Sancho, C., Soria, A.R. (Eds.) *Itinerarios Geológicos por Aragón*,
678 Sociedad Geológica de España, Zaragoza. *Geo-Guías* 1, 151-180.
- 679 Liesa, C.L.; Soria, A.R.; Meléndez, N., Meléndez, A., 2006. Extensional fault control on the
680 sedimentation patterns in a continental rift basin: El Castellar Formation, Galve sub-basin,
681 Spain. *Journal of the Geological Society, London* 163, 487-498.
- 682 Lisle, R.J., Orife, T. Arlegui, L.E., 2001. A stress inversion method requiring only fault slip
683 sense. *Journal of Geophysical Research* 106 (B2), 2281-2289.
- 684 Moissenet, E., 1983. Aspectos de la Neotectónica en la fosa de Teruel. In: Comba, J.A. (Ed.),
685 *Geología de España. Libro Jubilar J.M. Ríos, Vol. II. IGME. Madrid.* 427-446.
- 686 Navarrete, R., Liesa, C.L., Soria, A.R., Rodríguez-López, J.P., 2013. Actividad de fallas durante
687 el depósito de la Formación Camarillas (Barremiense) en la subcuenca de Galve (E de
688 España). *Geogaceta* 53, 61-64.

- 689 Paricio, J., Simón, J.L., 1986. Aportaciones al conocimiento de la compresión tardía en la
690 Cordillera Ibérica oriental: la cuenca neógena inferior del Mijares (Teruel-Castellón).
691 Estudios Geológicos 42, 307-319.
- 692 Peacock, D.C.P., Sanderson, D.J., 1991. Displacements, segment linkage and relay ramps in
693 normal fault zones. *Journal of Structural Geology* 13, 721–733.
- 694 Peña, J.L., Gutiérrez, M., Ibáñez, M.J., Lozano, M.V., Rodríguez, J., Sánchez-Fabre, M., Simón,
695 J.L., Soriano, M.A., Yetano, L.M., 1984. Geomorfología de la provincial de Teruel, Instituto
696 de Estudios Turolenses, 149 p.
- 697 Piromallo, C., Morelli, A., 2003. P-wave tomography of the mantle under the Alpine-Mediterra-
698 nean area. *Journal of Geophysical Research* 108 (B2), doi:10.1029/2002JB001757.
- 699 Reches, Z., 1978. Analysis of faulting in three-dimensional strain fields. *Tectonophysics* 47, 109-
700 129.
- 701 Reches, Z., Dieterich, J.H., 1983. Faulting of rocks in three-dimensional strain fields. I. Failure
702 of rocks in polyaxial, servo-control experiments. *Tectonophysics* 95, 111-132.
- 703 Rispoli, R., 1981. Stress fields about strike-slip faults inferred from stylolites and tension gashes.
704 *Tectonophysics* 75, 29–36.
- 705 Roca, E., Guimerà, J., 1992. The Neogene structure of the eastern Iberian margin: structural
706 constraints on the crustal evolution of the Valencia trough (western Mediterranean).
707 *Tectonophysics* 203, 203-218.
- 708 Rodríguez-López, J.P., Liesa, C.L., van Dam, J., Lafuente, P., Arlegui, L., Ezquerro, L., de Boer,
709 P.L., 2012. Aeolian construction and alluvial dismantling of a fault-bounded intracontinental
710 aeolian dune field (Teruel Basin, Spain); a continental perspective on late Pliocene climate
711 change and variability. *Sedimentology* 59, 1536-1567.

- 712 Rubio, J.C., Simón, J.L., 2007. Tectonic subsidence v. erosional lowering in a controversial
713 intramontane depression: the Jiloca basin (Iberian Chain, Spain). *Geological Magazine* 144,
714 1-15.
- 715 Scotti, V.N., Molin, P., Faccenna, C., Soligo, M., Casas-Sainz, A., 2014. The influence of
716 surface and tectonic processes on landscape evolution of the Iberian Chain (Spain):
717 Quantitative geomorphological analysis and geochronology. *Geomorphology* 206, 37-57.
- 718 Simón, J.L., 1982. Compresión y distensión alpinas en la Cadena Ibérica oriental. Ph.D. Thesis.
719 Publ. Inst. Estudios Turolenses, Teruel.
- 720 Simón, J.L., 1983. Tectónica y neotectónica del sistema de fosas de Teruel. *Teruel* 69, 21-97.
- 721 Simón, J.L., 1986. Analysis of a gradual change in stress regime (example from the eastern
722 Iberian Chain, Spain). *Tectonophysics* 124, 37-53.
- 723 Simón, J.L., 1989. Late Cenozoic stress field and fracturing in the Iberian Chain and Ebro Basin.
724 *Journal of Structural Geology* 11, 285-294.
- 725 Simón, J.L., Paricio, J., 1988. Sobre la compresión neógena en la Cordillera Ibérica. *Estudios*
726 *Geológicos* 44, 271-283.
- 727 Simón, J.L., Soriano, M. A. (1993). La falla de Concud (Teruel): actividad cuaternaria y régimen
728 de esfuerzos asociado. In: Aleixandre, T., Pérez González, A. (Eds.), *El Cuaternario de*
729 *España y Portugal*. ITGE, Madrid 2, 729-737.
- 730 Simón, J.L., Arenas, C., Arlegui, L., Aurell, M., Gisbert, P., Gonzalez, A., Liesa, C., Martin, C.,
731 Melendez, A., Melendez, G., Pardo, G., Soria, A.R., 1998. Guía del parque geológico de
732 Aliaga. Ayuntamiento de Aliaga, Centro para el Desarrollo del Maestrazgo, Departamento de
733 Geología de la Universidad de Zaragoza.

- 734 Simón, J.L., Arlegui, L.E., Liesa, C.L., Maestro, A., 1999. Stress perturbations registered by
735 jointing near strike-slip, normal, and reverse faults: Examples from the Ebro Basin, Spain.
736 *Journal of Geophysical Research (Solid Earth)* 104, 15141-15153.
- 737 Simón, J.L., Arlegui, L.E., Liesa, C.L. (2008) Stress partitioning: a practical concept for
738 analysing boundary conditions of brittle deformation. *Geodinamica Acta* 21, 107-115.
- 739 Simón, J.L., Arlegui, L.E., Lafuente, P., Liesa, C.L., 2012. Active extensional faults in the
740 central-eastern Iberian Chain, Spain. *Journal of Iberian Geology* 38, 127-144.
- 741 Simón, J.L., Arlegui, L.E., Ezquerro, L., Lafuente, P., Liesa, C.L., Luzón, A., 2017. Assessing
742 interaction of active extensional faults from structural and paleoseismological analysis: The
743 Teruel and Conclud faults (eastern Spain). *Journal of Structural Geology* 103, 100–119.
- 744 Simón, J.L., Liesa, C.L., Arlegui, L.E., Ezquerro, L., Luzón, A., Medialdea, A., 2018.
745 Paleoseismicity of the Valdecebro fault (Teruel basin, Iberian Chain). In: Canora, C. (Ed.).
746 *Avances en el estudio de fallas activas, terremotos y peligrosidad sísmica de Iberia. III*
747 *Reunión Ibérica sobre Fallas Activas y Paleosismología, Alicante (España)*, 115–118.
- 748 Soria, A.R., 1997. La sedimentación en las cuencas marginales del surco ibérico durante el
749 Cretácico Inferior y su control tectónico. Ph.D. Thesis, University of Zaragoza, Zaragoza, pp.
750 363.
- 751 Soria, A.R., Meléndez, M.N., Meléndez, A., Liesa, C.L., Aurell, M., Gómez Fernández, J.C.,
752 2000. The Early Cretaceous of the Iberian Basin (Northeastern Spain). In: Gierlowski-
753 Kordesch, E.H. and, Kelts, K.R. (Eds.). *Lake basins through space and time, AAPG studies in*
754 *Geology* 46, 285-294.
- 755 Walsh, J.J., Watterson, J., Bailey, W.R., Childs, C., 1999. Fault relays, bends and branch-lines.
756 *Journal of Structural Geology* 21, 1019–1026.

757 Weerd, A., 1976. Rodent faunas of the Mio-Pliocene continental sediments of the Teruel-
758 Alfambra region, Spain. Ph.D. Thesis. Utrecht Micropaleontol. Bulletin, Special Publication
759 2. Utrecht.
760

ACCEPTED MANUSCRIPT

761 **FIGURE CAPTIONS**

762 **Fig. 1.** (a) Location of the northern Teruel Basin within the eastern Iberian Peninsula. (b) Overall
 763 cross section of the northern Teruel half-graben.

764 **Fig. 2.** Synthetic structural map of the northern Teruel Basin showing the main faults at its
 765 eastern margin, as well as the prerift blocks cropping out in the eastern and western basin
 766 margins and in intrabasinal locations.

767 **Fig. 3.** Geological cross-sections along the northern sector of the Teruel Graben (see location in
 768 Figure 2). Fault throws are estimated from the *IES* and *FES* planation surfaces markers.

769 **Fig. 4.** Detailed map of fracture systems in Neogene and Mesozoic units in and around the
 770 central-northern Teruel Basin. Stereoplots represent fault orientations and stress axes obtained by
 771 Ezquerro (2017). Blue arrows indicate the azimuth of the σ_3 axis of extensional stress tensors.
 772 Red arrows indicate the azimuth of the σ_1 axis of compressional stress tensors. Numbers close to
 773 black dots refer to literature data (see Table 1), while those in white small circles refer to Table 2
 774 (Ezquerro, 2017).

775 **Fig. 5.** Frequency distribution of fracture directions in and around the central-northern Teruel
 776 Basin. (a), (b), (c): fractures in Mesozoic units. (d), (e), (f): fractures in Neogene units.
 777 Histograms represent accumulated fracture lengths for classes of 1°; the smoothed frequency
 778 curve (rolling average and window of 10°) is also shown. Rose diagrams represent the absolute
 779 number of fractures for classes of 10°, and they are elaborated for both the total fracture
 780 population and map-scale, > 2 km-long faults.

781 **Fig. 6.** Distribution of palaeostress directions (mainly tensile stress tensors) recorded in the
 782 central-northern Teruel Basin. (a) Synthetic y-R diagram of stress tensors for which the R stress
 783 ratio is available; the blue shadow displays the main clusters of horizontal σ_y azimuths ($\sigma_y = S_{Hmax}$
 784 = maximum horizontal stress, corresponding to σ_2 in all cases); $R = (\sigma_z - \sigma_x) / (\sigma_y - \sigma_x)$, Bott

785 (1959). (b) Histogram of total σ_3 azimuths recorded along the Late Miocene-Quaternary series,
 786 including those stress solutions with (in green) and without (in blue) R stress ratio; vertical pink
 787 bands correlate the relative maxima that are tentatively interpreted as the prevailing recent stress
 788 systems, as discussed in the text. (c) Separated histograms of σ_3 azimuths and chronological
 789 relationships according to the age of rocks where they are recorded.

790 **Fig. 7.** Detail of the zigzag fault arrangement of the northern El Pobo Fault Zone (EPFZ) (see
 791 Fig. 2 for location).

792 **Fig. 8.** Sketch showing the general evolution of the central-northern sector of the Neogene
 793 Teruel Basin. EPFZ: El Pobo Fault Zone; PF: Peralejos Fault; TF: Tortajada Fault; VFZ:
 794 Valdecebro Fault Zone; LHFZ: La Hita Fault Zone; TeF: Teruel Fault; CF: Conclud Fault; SPFZ:
 795 Sierra Palomera Fault Zone.

796 TABLE CAPTIONS

797 **Table 1.** Palaeostress results compiled from previous publications. 1: Lafuente (2011), 2: Arlegui
 798 et al. (2006), 3: Simón (1989), 4: Arlegui et al. (2005), 5: Liesa (2011), 6: Cortés (1999), 7:
 799 Simón and Paricio (1988). Extensional and compressional stress tensors are distinguished. The
 800 following information is given for each data site: acronym used in the present work, in particular
 801 in Figure 4; name or acronym from the original publication; UTM coordinates, X and Y; affected
 802 rocks (Lm: limestone, Gy: gypsum, Mu: mudstone, St: sandstone, Co: conglomerate); age;
 803 lithostratigraphic unit according to Godoy et al. (1983a,b) (CL: Cuevas Labradas Fm., UDI:
 804 *Unidad Detrítica Inferior-Rojo 1*, CI: *Calizas Intermedias*, P1: *Páramo 1*, P2: *Páramo 2*, R3:
 805 *Rojo 3*, VP: *Villafranchian Pediment*); genetic unit according to Ezquerro (2017); azimuth of the
 806 horizontal σ_3 axis (extensional tensors) or the horizontal σ_1 axis (compressional tensors); stress
 807 ratio R_e used by Etchecopar et al. (1981); stress ratio R used by Bott (1959); (1), (2), (3) indicate
 808 chronological order of stress tensors; mean *angular misfit* ($^\circ$) between observed slip and the

809 resolved shear stress from the computed stress solution; number of explained faults (n) in
810 relation with the total number of faults of the site, and analytical method used for stress inversion
811 (ET: Etchecopar's method, yR: y-R diagram method, Li: Lisle et al. (2001) method).

812 **Table 2.** Palaeostress results obtained by Ezquerro (2017); extensional and compressional stress
813 tensors are distinguished. The following information is given for each data site: label used in the
814 present work, in particular in Fig. 4; name according to Ezquerro (2017); UTM coordinates,
815 affected rocks, age, lithostratigraphic and genetic unit, azimuth of the horizontal σ_3 or σ_1 axis,
816 stress ratio, chronological order, and analytical method, as in Table 1; n/N: number of data
817 explained by the stress tensor with respect to the total sample size.

Site		Location		Lithology	Age	Unit		Stress state			Angular misfit	n/N	Analysis method	
Ref	Nº	Original name	Coord. X			Coord. Y	1	2	Azimet	R _e				R
Extensional stress tensors (σ_1 vertical)						σ_3								
1	P1	A01	661867	4470590	Lm	Turolian	P1	TN3	056	0.32	3.13	5°	11/15	ET
	P2	A02	661888	4470548	Lm	Turolian	P1	TN3	170	0.18	5.56	8°	7/9	ET
	P3	A03	661903	4470523	Lm	Turolian	P1	TN3	008	0	+∞	4°	12/16	ET
	P4	A04	661928	4470419	Lm	Turolian	P1	TN3	093	0.05	20.0	7°	9/11	ET
	P5	A05	661984	4470426	Lm	Turolian	P1	TN3	062	0.35	2.86	-	18/18	ET
	P6	A06	661201	4470221	Lm + Gy	Vallesian	Cl	TN2	172 (1)	0	+∞	10°	21/47	ET
					Lm				064 (2)	0.02	50.0	10°	13/47	ET
	P7	A07	662042	4470368	Lm	Turolian	P1	TN3	099	0.03	33.3	9°	20/24	ET
	P8	A08	662211	4470339	Lm	Turolian	P1	TN3	036	0.03	33.3	6°	20/25	ET
	P9	A09	661621	4470022	Lm	Ruscinian	P2	TN4	122	0.09	11.1	5°	20/22	ET
	P10	A10	661663	4469924	Lm	Ruscinian	P2	TN4	098	0.08	12.5	7°	22/27	ET
	P11	A11	661447	4469112	Lm	Ruscinian	P2	TN4	110	0.07	14.2	2°	10/21	ET
	P12	A12	661882	4468510	Lm + Gy	Turolian	P1	TN3	133	0.01	100	10°	9/13	ET
	P13	A13	661312	4468977	Lm + Gy	Ruscinian	P2	TN4	138	0.16	6.25	14°	15/22	ET
	P14	A14	662438	4468363	Lm	Turolian	P1	TN3	126	0.05	20.0	8°	19/28	ET
	P15	A15	661078	4468654	Lm	Ruscinian	P2	TN4	034	0.03	33.3	7°	25/26	ET
	P16	A16	663053	4468219	Lm + Gy	Ruscinian	P2	TN4	049	0.03	33.3	8°	24/32	ET
	P17	T01	661519	4466583	Lm	Vallesian	UDI	TN2	094	0.10	10.0	-	8/8	ET
2	P18	04	653231	4472974	Co	Villafranchian	VG	TN5	000				39/39	LI
	P19	06	657728	4473332	Co + St	Villafranchian	VG	TN5	126 (1)				14/22	LI
									036 (2)				8/22	LI
	P20	07	657718	4472645	Co + Mu	Villafranchian	VG	TN5	022				50/50	LI
	P21	08	661805	4471587	Lm	Turolian	P1	TN3	146				12/12	LI
	P22	10	661452	4471286	Lm	Turolian	P1	TN3	075				8/8	LI
	P23	11	661452	4471286	Lm	Turolian	P1	TN3	071				11/11	LI
	P24	12	661452	4471286	Lm	Turolian	P1	TN3	015				13/13	LI
	P25	13	661452	4471286	Lm	Turolian	P1	TN3	175				11/11	LI
	P26	14	661452	4471286	Lm	Turolian	P1	TN3	090				16/16	LI
	P27	15	660822	4470257	Co	Villafranchian	R3	TN5	042				13/13	LI
	P28	16	659316	4472974	Lm	Turolian	P1	TN3	035				22/22	LI
	P29	17	661328	4472049	Lm	Turolian	P1	TN3	065				33/33	LI
	P30	18	659945	4470729	Mu	Villafranchian	R3	TN5	166				20/20	LI
3,6	P31	Orrios	668712	4494100	Lm	Ruscinian	P2	TN4	056 (1)	0.40	2.50	7°	12/58	ET
									112 (2)	0.20	5.00		9/58	yR
4	P32	12 Perales	670230	4502076	Co	Villafranchian	VG	TN5	067				10/10	LI
	P33	13 Villalba Alta 1	671947	4497718	Lm	Villafranchian	R3	TN5	004				24/24	LI
	P34	15 Escorihuela	672958	4487361	Co	Villafranchian	VG	TN5	075				14/14	LI
	P35	19 Valdecebro	671899	4469660	Co	Villafranchian	VG	TN5	072				12/12	LI
5	P36	Pobo 3	674717	4495591	Lm	Early Jurassic	CL		027	0.03	33.3	12°	7/9	ET
	P37	Pobo 5	676968	4493436	Lm	Early Jurassic	CL		120	0.50	2.00		2/17	yR
	P38	Pobo 7	675738	4487342	Lm	Early Jurassic	CL		124 (1)	0.45	2.22	12°	15/51	ET
									010 (2)	0.22	4.50	3°	6/51	ET
	P39	Pobo 8	677388	4487342	Lm	Early Jurassic	CL		096	0.40	2.50		7/37	yR
	P40	Pobo 9	676787	4485387	Lm	Early Jurassic	CL		107	0.24	4.17	11°	18/42	ET
6	P41	567/06	663200	4469600	Lm	Turolian	P1	TN3	102	0.14	7.14	6°	8/11	ET
	P42	567/07	658400	4478200	Lm + Mu	Villafranchian			040				10/10	LI
4		08 Caudé			Co	Villafranchian	VG	TN5	000				25	LI
		09 Bco. del Monte			Co + St	Mid. Pleistoc.	T		073				32	LI
		11 Conclud 2			Co + Mu	Villafranchian	VG	TN5	022				38	LI
		14 Orrios			Co + St	Mid. Pleistoc.	T		175				35	LI
		16 Los Baños 1			Co	Mid. Pleistoc.	T		145				10	LI
		17 Los Baños 2			Co	Mid. Pleistoc.	T		053				10	LI
		18 Teruel			Co + St	Mid. Pleistoc.	T		066				13	LI
2		01			Mu + Co	Villafranchian	VG	TN5	073				28	LI
		02			Mu + Co	Villafranchian	VG	TN5	065				26	LI
		03			Co	Villafranchian	VG	TN5	066				26	LI
		05			Co + Mu	Mid. Pleistoc.	T		073				35	LI
		09			Co	Mid. Pleistoc.	T		057				12	LI
		19			Co + Mu	Mid. Pleistoc.	T		066				23	LI
Compressional and strike-slip stress tensors (σ_1 horizontal)						σ_1								
6,7	P31	Orrios	668712	4494100	Lm	Ruscinian	P2	TN4	033 (1)	0.96	0.96	9°	11/58	ET
									001 (2)	0.52	0.52	8°	8/58	ET

TABLE 1

Site		Location		Lithology	Age	Unit		Stress state			Angular misfit (°)	n°/ N	Analysis method
N°	Name	Coord. X	Coord. Y			1	2	Azimuth	R _e	R			
Extensional stress tensors (σ_1 vertical)													
						σ_3							
1	Alcamines río	673795	4500189	Mu + St	Vallesian	UDI ?	086	0.58	1.72		6°	11/17	ET
2	Villalba Alta macroestación	673265	4498417	Mu + Co	Late Ruscinian	UDI TN5	087	0	$\rightarrow\infty$			20/36	LI
3	Villalba Alta granja	672271	4498208	Lm	Late Ruscinian	P2 TN4	125 (1)	0	$\rightarrow\infty$		8°	25/35	ET
							089 (2)	0	$\rightarrow\infty$		10°	26/35	ET
5	Corral del Majano	662718	4490981	Co	Vallesian	UDI TN1	135	0	$\rightarrow\infty$			16/21	LI
6	Corrales de Cabigordo	663273	4487905	Mu + Co	Vallesian	UDI TN1	062	0	$\rightarrow\infty$			7/14	LI
7	Bco. Hondo	671492	4484088	Co	Early Turolian	UDI TN4	124	0.05	20.00			12/12	LI
8	Muela umbria norte	665827	4488356	Lm	Turolian	P1 TN3	121	0.07	14.29		12°	15/21	ET
9	Peralejos merendero	666871	4483058	Lm	Vallesian	KI TN2	176 (1)	0.07	14.29		8°	10/28	ET
							095 (2)	0.07	14.29			26/28	ET
10	Venta Alta	666070	4483597	Lm	Early Ruscinian	P2 TN4	040	0	$\rightarrow\infty$		8°	14/17	ET
11	Cueva Tinajo	668321	4483983	Lm	Turolian	P1 TN3	016	0.03	33.33		10°	22/27	ET
12	Cañamaria	656953	4480493	Lm	Early Ruscinian	P2 TN4	111	0.05	20.00		7°	25/27	ET
13	Sta. Quiteria afluente	663772	4479859	Lm	Early Ruscinian	P2 TN4	085	0.15	6.67		10°	16/18	ET
14	Sta. Quiteria calizas	663762	4479949	Lm	Late Turolian	R2 TN4	136 (1)	0.04	25.00		6°	15/25	ET
							085 (2)	0.05	20.00		8°	14/25	ET
15	Sta. Quiteria margas	663762	4479949	Lm	Late Turolian	R2 TN4	178 (1)	0	$\rightarrow\infty$			17/20	LI
							034 (2)	0.12	8.33		6°	7/9	ET
16	Bco. de los Chopos	663643	4478853	Mu + Lm	Late Turolian	R2 TN4	090	0.04	25.00			9/15	LI
17	Villalba Baja delta IV	663390	4477501	Mu + Lm	Late Turolian	R2 TN4	058	0	$\rightarrow\infty$			8/14	LI
18	Villalba Baja delta III	663385	4477496	Mu + Lm	Late Turolian	R2 TN4	038	0	$\rightarrow\infty$			16/21	LI
19	Villalba Baja delta II	663362	4477480	Mu + Lm	Late Turolian	R2 TN4	019					4/4	CF
20	Villalba Baja delta I	663334	4477442	Mu + Lm	Late Turolian	R2 TN4	025	0.05	20.00			21/29	LI
21	Villalba Baja rio	663195	4476871	Mu + Lm	Turolian	P1 TN2	046	0.02	50.00			27/34	LI
22	Mas de la Casa Baja	672446	4471615	Co	Vallesian	UDI ?	121	0	$\rightarrow\infty$			8/17	LI
23	Valdecebro Talud	664431	4469654	Mu	Vallesian	UDI TN1	087 (2)	0.33	3.03		5°	6/23	ET
							058 (3)	0.03	33.33			24/41	LI
24	Cuevas de las Tres Puertas	661796	4468275	Lm + Gy	Turolian	P1 TN3	058	0.17	5.88		11°	17/23	ET
Compressional and strike-slip stress tensors (σ_1 horizontal)													
						σ_1							
4	Castillo de Alfambra	666125	4490261	Mu	Vallesian	UDI TN3	027	0.74	-2.85			6/11	LI
23	Valdecebro Talud	664431	4469654	Mu		UDI TN1	166 (1)	0.86	0.86		8°	12/23	ET

TABLE 2

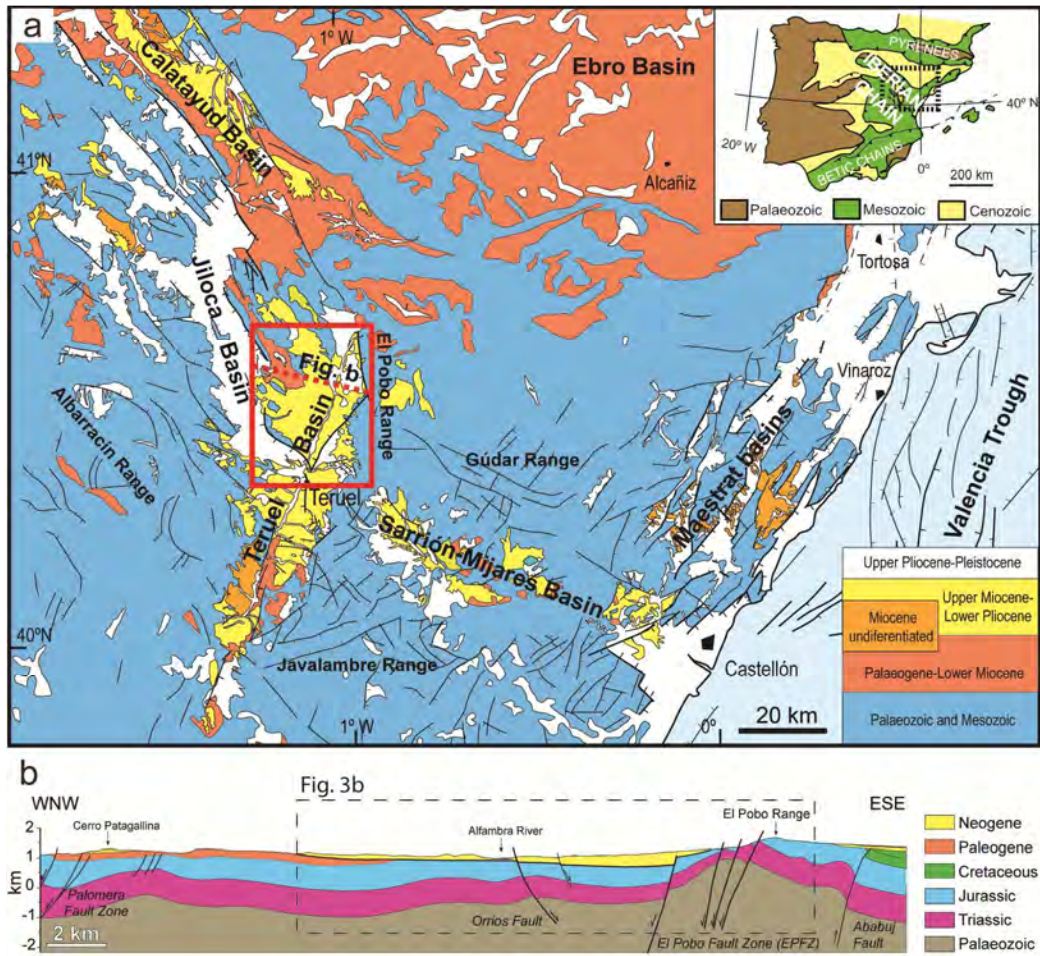


Figure 1

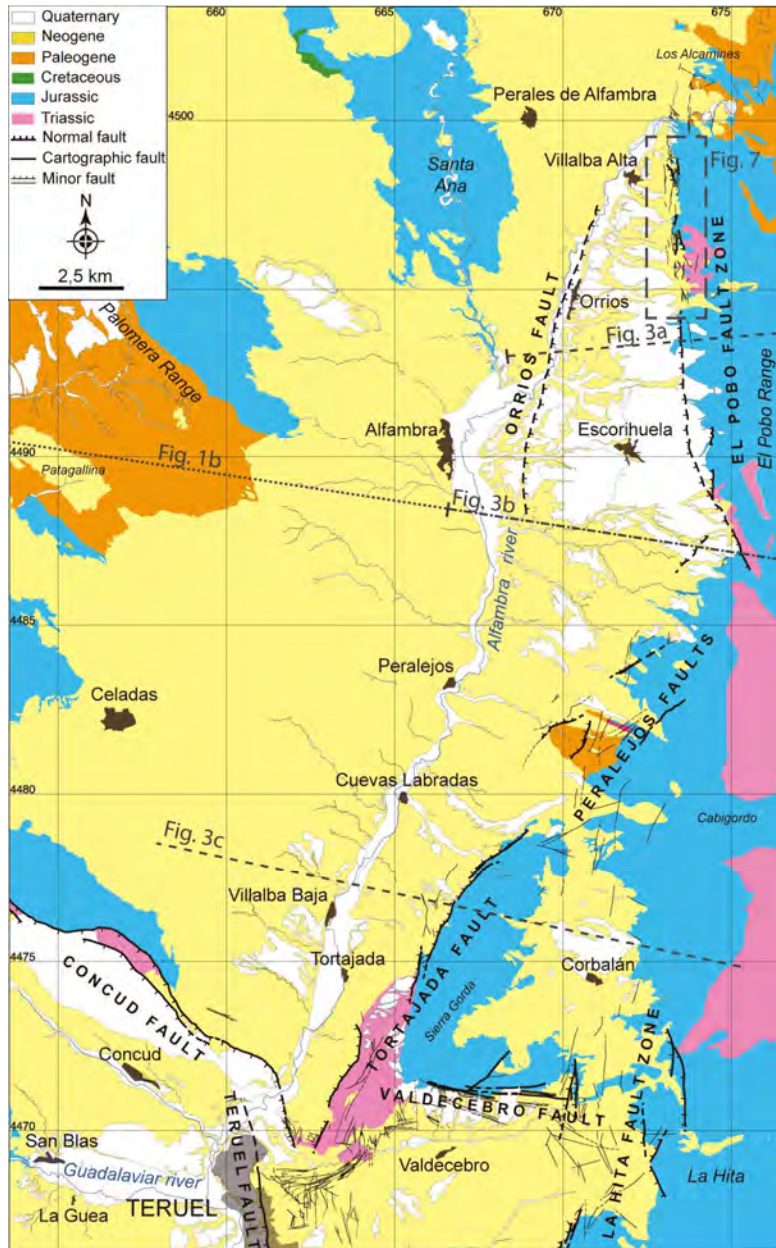


Figure 2

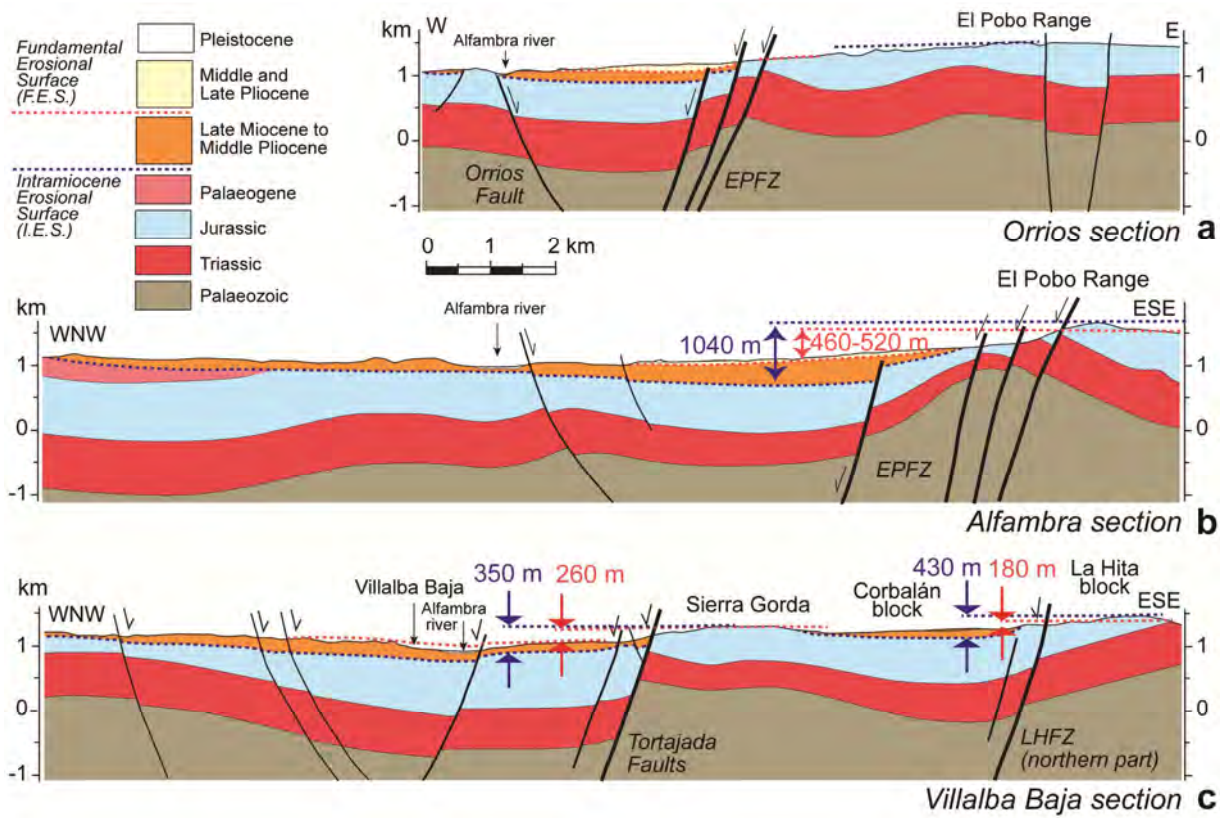
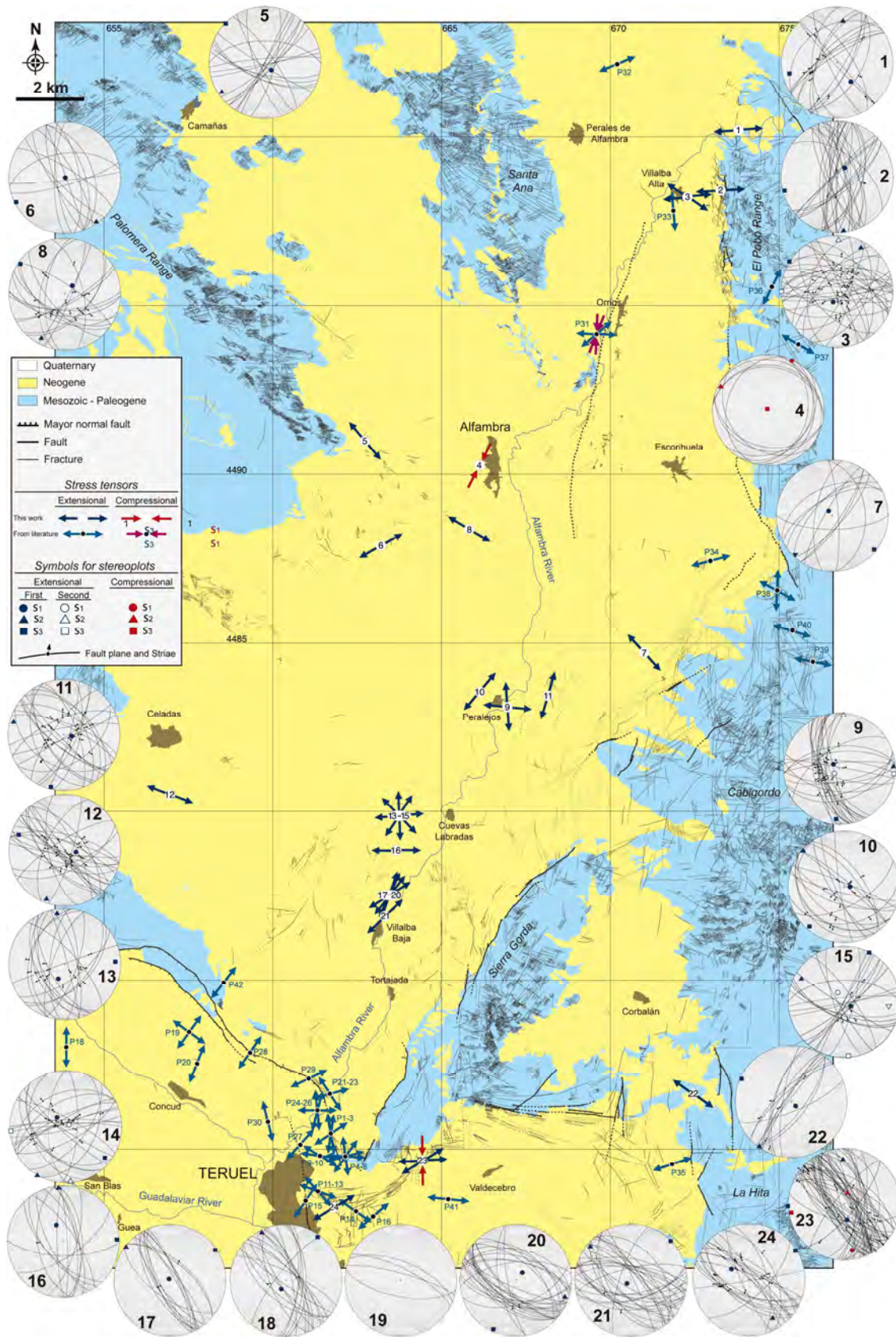


Figure 3



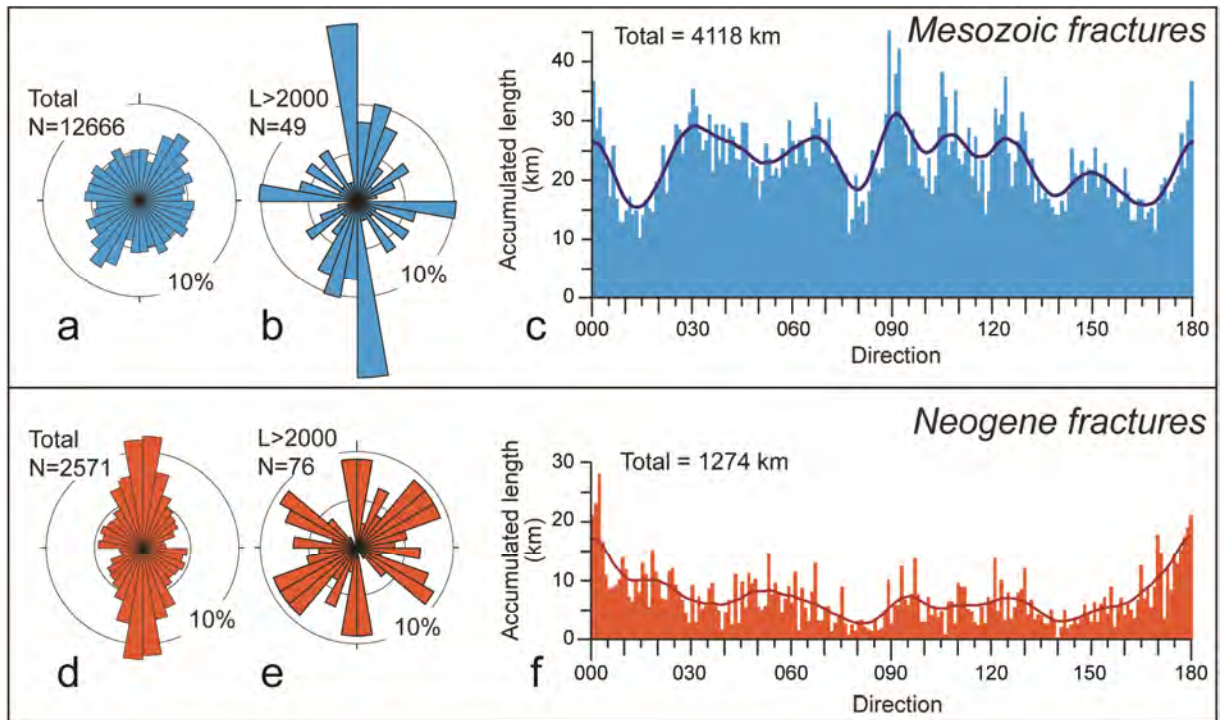
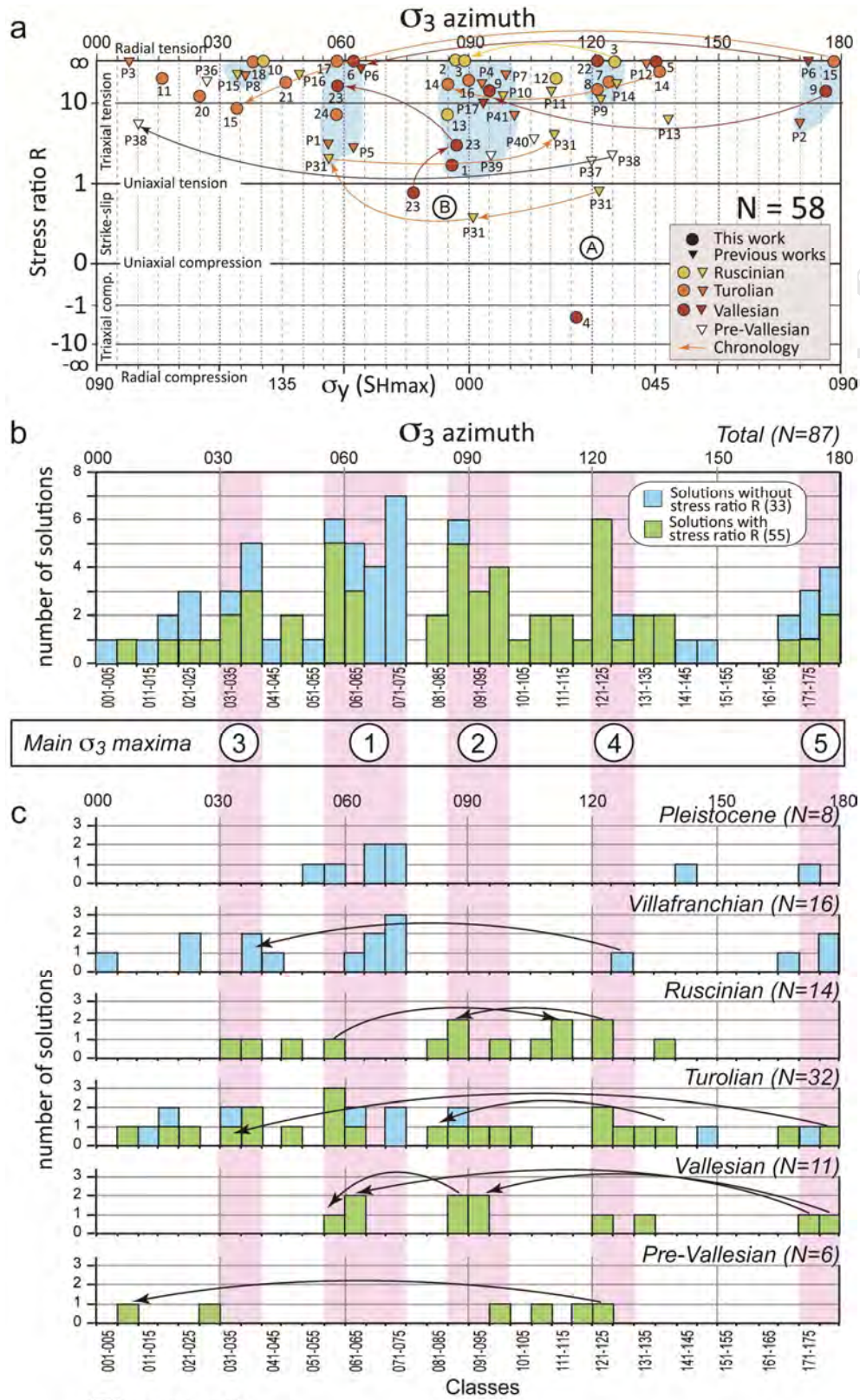
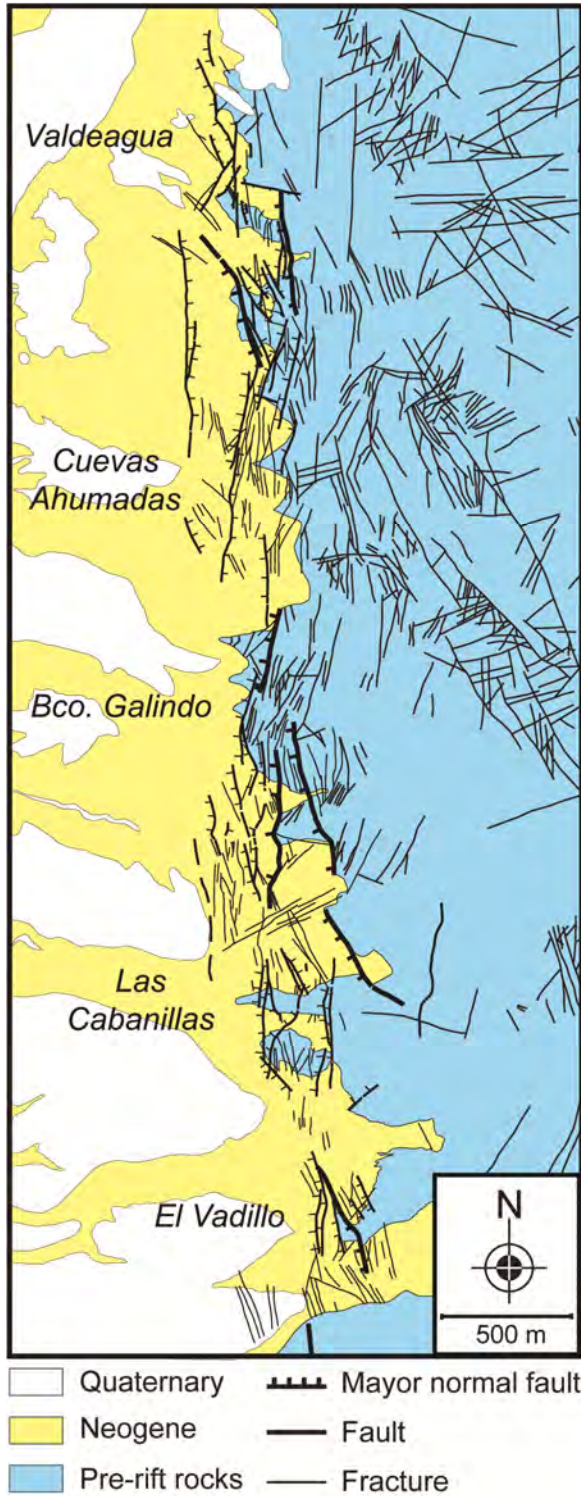


Figure 5



*Figure 7*

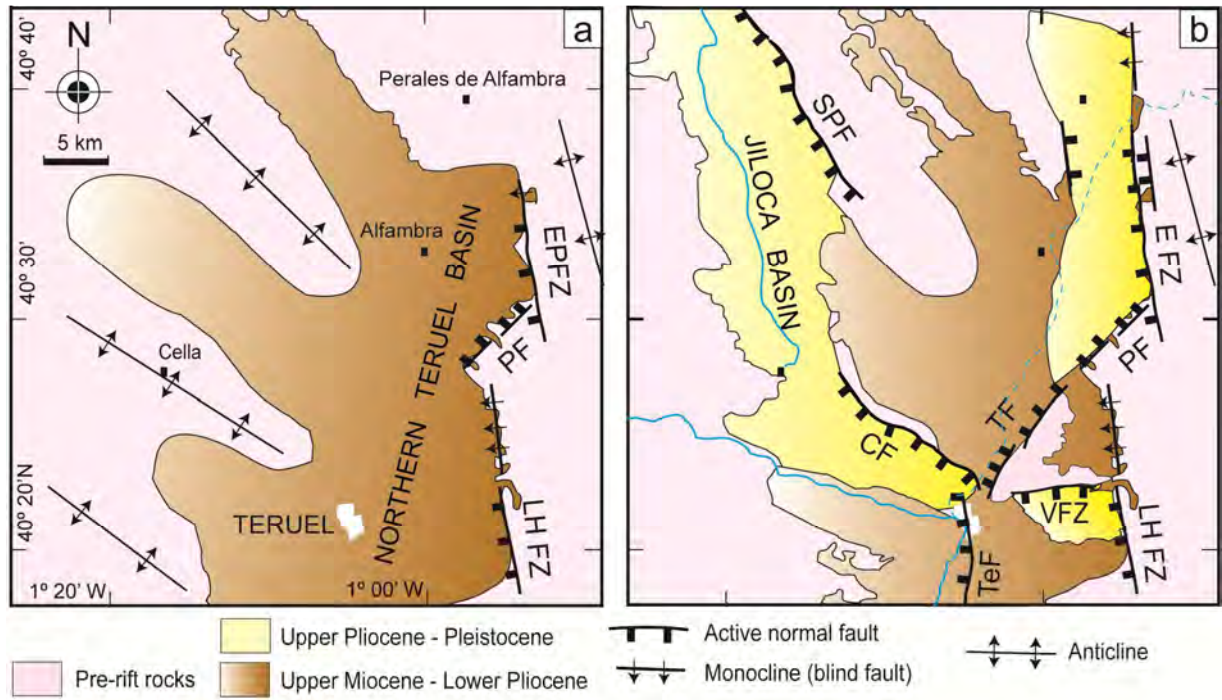


Figure 8

Highlights

Diverse orientation, border and intrabasinal faults in the Neogene Teruel basin.

Use of stratigraphical–geomorphological markers for analysing fault activity.

Characterization of Neogene deformation and structural inheritance from fracturing.

Structural inheritance and evolving stress systems as controls on basin evolution.